BNL-229515-2026-JAAM

Metabolic flux, metabolite, and transcript analysis uncover reprogramming of metabolism toward higher seed oil

H. Shi

To be published in "Plant Physiology"

February 2026

Biology Department

Brookhaven National Laboratory

U.S. Department of Energy

USDOE Office of Science (SC), Basic Energy Sciences (BES)

DISCLAIMER

Metabolic flux, metabolite, and transcript analysis uncover reprogramming of metabolism toward higher seed oil

Hai Shi[1], Michaela McGinn[2], Nathaphon Yu King Hing[1*], Brice A. Jarvis[2], Barsanti Gautam[2], Cathleen Kuczynski[1], Alexander Hilo[3], Hardy Rolletschek[3], John C. Sedbrook[2], Jorg Schwender[1#]

[1]Department of Biology, Brookhaven National Laboratory, Upton, NY 11973, USA;
[2]School of Biological Sciences, Illinois State University, Normal, IL 61790, USA;
[3]Leibniz-Institute of Plant Genetics and Crop Plant Research (IPK), Corrensstrasse 3, Seeland, OT Gatersleben, 06466, Germany

*Present contact joel.ykh@gmail.com

#Corresponding author: Jorg Schwender, E-mail: schwend@bnl.gov

The author responsible for distribution of materials integral to the findings presented in this article in accordance with the policy described in the Instructions for Authors (https://academic.oup.com/plphys/pages/General-Instructions) is Jorg Schwender.

Running title: WRI1 and DGAT1 overexpression in pennycress embryos

Abstract

Overexpression of *WRINKLED1* (*WRI1*), a master regulator of glycolysis and fatty acid biosynthesis, together with *DIACYLGLYCEROL ACYLTRANSFERASE1* (*DGAT1*), which catalyzes the final step of triacylglycerol assembly, is a promising strategy for enhancing seed oil content. However, how these regulators coordinate system-wide metabolic reprogramming at the levels of gene expression, metabolite pools, and fluxes remains poorly understood. To address this, we performed ^{13}C-metabolic flux analysis, metabolomics, and transcriptomics on in vitro cultured pennycress (*Thlaspi arvense* L.) embryos overexpressing the native *WRI1* and *DGAT1* homologs. In cultured embryos, *WRI1*/*DGAT1* overexpression increased triacylglycerol accumulation by 28% while reducing protein content by 34%, relative to the wild type. Embryos showed ~20-fold and 50-fold upregulation of *WRI1* and *DGAT1* along with induction of WRI1 target genes in glycolysis and fatty acid biosynthesis. Genes associated with photosynthesis and Calvin cycle functions were also upregulated, whereas genes encoding ribosomal proteins and seed storage proteins were strongly repressed, consistent with the observed lipid–protein tradeoff. Flux analysis revealed that enhanced triacylglycerol biosynthesis is supported by increased flux through the Rubisco shunt and cytosolic pyruvate kinase, while the oxidative pentose phosphate pathway and malic enzyme contributed little to NADPH or pyruvate supply. Metabolomic profiling revealed extensive perturbations in glycolytic intermediates, tricarboxylic acid cycle metabolites and amino acids. In plant grown seeds, *WRI1*/*DGAT1* lines also showed a modest but significant increase in total lipid content. Collectively, these findings reveal how WRI1 and DGAT1 reprogram central metabolism to enhance oil accumulation, with relevance to mature seeds.

Keywords: Diacylglycerol acyltransferase, metabolic flux analysis, metabolic engineering, pennycress, triacylglycerol, WRINKLED1.

Introduction

Plant oils are valuable commodities with wide-ranging applications as food, biofuels, and industrial feedstocks (Dyer et al., 2008). The commercial value of oilseeds is largely determined by the oil content as well as the protein and carbohydrate content. Increasing seed oil content depends on understanding how the carbon and nitrogen precursors received by a developing seed are partitioned into the major storage components: carbohydrates, protein, and oil. Elucidating the metabolic basis of this partitioning is a topic of great interest.

In developing seeds of various species, the expression of multiple genes associated with the lower section of the glycolysis pathway and fatty acid synthesis (FAS) is controlled by the master transcription factor *WRINKLED1* (*WRI1*) (Focks and Benning, 1998; Baud et al., 2007; Baud et al., 2009; Maeo et al., 2009; To et al., 2012; Fukuda et al., 2013; Kim et al., 2016; Kuczynski et al., 2022). In *Arabidopsis thaliana*, null mutants in *WRI1* were found to have significantly decreased seed oil content (Focks and Benning, 1998; Baud et al., 2007; Lonien and Schwender, 2009). Overexpression of *WRI1* homologs in a seed specific way resulted in increased total lipid or triacylglycerol (TAG) contents in seeds of Arabidopsis (Cernac and Benning, 2004; Liu et al., 2010; van Erp et al., 2014; Li et al., 2022), *Camelina sativa* (An and Suh, 2015), *Brassica napus* (Wu et al., 2014; Li et al., 2015), *Brasssica juncea* (Bhattacharya et al., 2016), *Lepidium campestre* (Ivarson et al., 2016), *Linum usitatissimum* (Li et al., 2022), *Glycine max* (Chen et al., 2018; Guo et al., 2020) or *Gossypium hirsutum* (Butt et al., 2024).

Downstream of FAS, TAG biosynthesis proceeds via sequential acylation steps catalyzed by glycerol-3-phosphate acyltransferase (GPAT), lysophosphatidic acid acyltransferase (LPAAT), phosphatidic acid phosphatase (PAP), and diacylglycerol acyltransferase (DGAT) (Li-Beisson et al., 2013; Chen et al., 2022). In parallel, acyl editing moves fatty acids among diacylglycerol, phosphatidylcholine, free fatty acids, and acyl-CoA, facilitating modification such as desaturation (Bates and Browse, 2012). A key enzyme responsible for the incorporation of newly formed fatty acids into TAG is DGAT1 (Jako et al., 2001; Zhang et al., 2009). Overexpression of Arabidopsis DGAT1 has been used successfully to increase seed oil content (Jako et al., 2001; Misra et al., 2013; Roesler et al., 2016; Weselake et al., 2024).

As a promising metabolic engineering strategy, the combined overexpression of *WRI1* and *DGAT1* is expected to coordinately upregulate multiple gene targets along the pathway converting sugars into TAG, spanning glycolysis, FAS, and TAG assembly. The effects of *WRI1*/*DGAT* overexpression have been reported two times for oilseeds (van Erp et al., 2014; Arias et al., 2022). In *Arabidopsis* seeds, combined overexpression of *AtWRI1* and *AtDGAT1* resulted in increased seed oil above the increases of the separate parent lines (van Erp et al., 2014), while in soybean, combined expression of *AtWRI1* and *AtDGAT1* altered oil and carbohydrate composition without increasing total fatty acid content in mature seeds relative to wild type (WT) (Arias et al., 2022).

In this study, we applied this strategy to pennycress (*Thlaspi arvense L.*). Pennycress has recently emerged as a promising oilseed intermediate crop (Altendorf et al., 2019; McGinn et al., 2019), yet efforts to increase its seed oil content remain limited (Lee et al., 2024; Gautam et al., 2025). While *WRI1* and *DGAT1* are established targets for enhancing oil accumulation in other species, their combined overexpression has not been tested in pennycress, and more broadly, how this strategy reprograms carbon and nitrogen metabolism during seed development is poorly understood. We hypothesized that simultaneous overexpression of *WRI1* and *DGAT1* would redirect carbon flux toward triacylglycerol synthesis at the expense of other biomass components. To test this, we carried out an integrated analysis of in vitro–cultured developing embryos using transcriptomics, metabolomics, and ^{13}C Metabolic Flux Analysis (^{13}C-MFA). ^{13}C-MFA quantifies in vivo flux in central metabolism (Kruger et al., 2011; O'Grady et al., 2012; Allen, 2016; Clark et al., 2020) and has been successfully applied before to cultures of developing embryos of other Brassicaceae species (Lonien and Schwender, 2009; Schwender et al., 2015; Carey et al., 2020). The combined approach allowed us to probe how central metabolic networks are reshaped by

WRI1/DGAT1 activity, thereby providing mechanistic insights into the regulation of carbon partitioning in the developing embryo with relevance to the mature pennycress seed.

Results

Identification of WRI1 and DGAT1 in pennycress

Using *Arabidopsis thaliana* (Arabidopsis) *WRI1* (*AtWRI1*; AT3G54320.1) and *DGAT1* (*AtDGAT1*, AT2G19450.1) coding sequences as the queries, we searched the pennycress genome sequence available at http://pennycress.umn.edu and a pennycress Transcriptome Shotgun Assembly (GAKE00000000) (Dorn et al., 2013), both of which are now available at the National Center for Biotechnology Information (NCBI), using a the Basic Local Alignment Search Tool (BLAST) program version 2.6.0+ (Zhang et al., 2000). These searches identified pennycress homolog genome regions as well as transcript sequences GAKE01001447.1 and GAKE01013486.1 for *TaWRI1* and *TaDGAT1*, respectively. The transcript sequences include ORFs with 1308 and 1569 nucleotides that align with 87% and 90% nucleotide sequence identity to the *WRI1* and *DGAT1* Arabidopsis coding sequences, respectively. In the pennycress v2 annotated genome (Nunn et al., 2022) *TaWRI1* and *TaDGAT1* identify with the gene locus IDs TAV2_LOCUS16256 and TAV2_LOCUS8955, respectively. Alignments of protein sequences are shown in Supplementary Figure S1 and Supplementary Figure S2. In order to increase lipid accumulation in pennycress seeds, endogenous *Ta*WRI1 and *Ta*DGAT cDNAs were cloned and ligated into vector pBinGlyRed3 (Zhang et al., 2013; Kim et al., 2015) for seed specific expression under control of the *Glycine max* glycinin promoter. After crossing of independent homozygous lines, four homozygous TaWRI1/TaDGAT1 (WD) lines were obtained (see methods). Lines WD3 and WD4 derive from independent parent events.

Dry seeds of TaWRI1 and TaDGAT1 overexpressing line have increased lipid content

To determine the effect of combined overexpression of *WRI1* and *DGAT1* on seed composition, mature seeds of lines WD3 and WD4 were analyzed by biomass fractionation and subsequent protein and starch determinations (methods, See Supplementary Table S1). Figure 1A shows an increase in total lipid and TAG by 5.9 and 10.3 % in WD3 compared to WT, while the proportion of polar methanol/water soluble metabolites (free metabolites) decreased. Similar increase in total lipid and TAG was seen in line WD4 (Figure 1B). For total seed weight per plant no significant change could be detected, indicating that the total seed yield is not affected in the transgenic (Supplementary Table S1). Majorly abundant fatty acids identified in WT, WD3 and WD4 mature seeds were palmitic acid (C16:0), oleic acid (C18:1), linoleic acid (C18:2) and α-linolenic acid (C18:3), as well as very long chain fatty acids (VLCFAs) of 20 carbon chain length and above, mostly gondoic acid (C20:1), erucic acid (C22:1) and nervonic acid (C24:1) (Figure 1C, D). Almost all fatty acid species differ significantly between WT and WD lines (Figure 1C, D). In WT seeds C22:1 was the most highly abundant fatty acid at close to 35 mol% (Figure 1C, D) as found before for pennycress WT spring32 (Jarvis et al., 2021; Claver et al., 2024). To estimate the metabolic fate of the main product of the plastidic FAS (C18:1), we derived the fatty acid desaturation ratio (FADR) and fatty acid elongation ratio (FAER) from the fatty acid profiles in similar to Velasco *et al.* (Velasco et al., 1998) (See methods). The FADR indicates how much C18:1 is converted into polyunsaturated fatty acids via the phosphatidyl choline and cytosol/ER bound unsaturation pathway (Li-Beisson et al., 2013). Accordingly, 33.9 mol% (WT) and 36.1 mol% (WD3) of C18:1 entered the desaturation pathway (Figure 1C), reflecting a modest increase in desaturation in WD3. A comparable increase in FADR was also observed in WD4 relative to WT (Figure 1D). The FAER indicates extension of C18 to VLCFAs via the cytosolic elongation pathway (Li-Beisson et al., 2013). Accordingly, FAER values show that 54.0 mol% (WT) and 53.4 mol%

(WD3) of C18 fatty acids were elongated into VLCFAs (Figure 1C). For WT and WD4, FAER values were 56.8 mol% and 55.4 mol%, respectively (Figure 1D), indicating a slight reduction in elongation activity in WD4.

Cultured WD3 embryos have increased lipid and decreased protein content

To assess the effect of *WRI1* and *DGAT1* overexpression on lipid accumulation, embryos from lines WD1, WD2, WD3, and WD4 were dissected ~15 days after flowering and cultured in liquid medium under controlled light and temperature (Methods). After 10 days, biomass fractionation revealed that all four transgenic lines exhibited a 21–33% increase in lipid content (Supplementary Figure S3). Repeated experiments confirmed that both WT and WD3 embryos continued to grow steadily for at least 10–14 days in culture (Supplementary Table S2). Based on these results, line WD3 was selected for more detailed characterization. Dry weight composition analysis after 10 days showed that WD3 embryos contained 31% more total lipid and 28% more TAG than WT, while protein content was reduced by 34% (Figure 2; Supplementary Table S3). These findings demonstrate that overexpression of *TaWRI1* and *TaDGAT1* substantially enhances lipid synthesis in cultured embryos, primarily at the expense of protein, consistent with a lipid–protein tradeoff. Like in the mature seeds, the fatty acid profile changed significantly between WT and WD3 embryos (Figure 2B). In both WT and WD3 embryos, the proportion of C18:1 is substantially higher compared to mature seeds, indicating that in cultured embryos less of this primary FAS product is subject to desaturation or elongation. Comparing WT and WD3 embryos, the FADR did not change significantly (Figure 2B), but the FAER shows that, relative to WT embryos, in WD3 the fraction of C18 fatty acids that were elongated into VLCFAs was reduced from 43.5 to 36.4 mol% (Figure 2B). The increased total lipid and TAG levels in WD3 and the reduced elongation activity together suggest that in WD3 the cytosolic elongation of C18 fatty acids to VLCFAs cannot keep pace with the increased synthesis rate of C18:1.

Overall, the increases in total lipids and TAG observed in WD3 embryos mirror the trends seen in dry seeds (Figure 1A), but are more pronounced in the cultured system. Similarly, WD3 embryos show a reduction in elongation to VLCFAs that is stronger than the effects in mature seeds (Figure 1C, D). These metabolic shifts are consistent with the flux analysis presented below. Notably, however, the reduction in protein content detected in WD3 embryos was not observed in dry seeds. This discrepancy likely reflects the fact that in vitro culture does not fully recapitulate the developmental program occurring in planta, a conclusion that is supported by the analysis of transcriptome profiles described in the following section.

The transcriptome profiles of cultured embryos have closest similarity to in planta grown seeds 12 days after flowering

To further characterize the lipid-protein tradeoff between WD3 and WT cultured embryos, we investigated how this trade-off between biomass components relates to changes in gene expression. WD3 and WT embryos cultured for 10 days were compared using whole-transcriptome sequencing (mRNA-seq). Using the pennycress annotated genome by Nunn *et al.* (Nunn et al., 2022) as a reference, gene expression values were obtained for 27,148 gene loci and overall, 97.3% of the reads were successfully aligned to the reference genome (Supplementary Table S4). Using Principal Component Analysis, we compared the WT and WD3 transcriptome data to a transcriptome time series for developing pennycress (inbred parent Spring32-10) seeds by Claver *et al.* (Claver et al., 2024). In result, the transcriptomes of both WT and WD3 have closest similarity to stage 1 in seed development at 12 days after flowering (DAF) (Supplementary Figure S4A). This developmental stage corresponds to peak expression of *WRI1* and several of its downstream targets involved in fatty acid biosynthesis (Supplementary Figure S4B). In contrast, transcripts associated with later lipid-modification steps—such as *TaDGAT1*, *TaFAE1* (Jarvis et al., 2021), and *TaFAD2* (Jarvis et al., 2021)—increase after 12 DAF in planta (Supplementary Figure S4C).

Likewise, seed-storage albumin and globulin transcripts accumulate primarily between 20 and 30 DAF (Supplementary Figure S4C). These patterns indicate that the cultured embryos correspond to an early developmental phase characterized by strong fatty acid biosynthetic activity, prior to the onset of major storage protein accumulation in planta.

Genes in lipid metabolism and other metabolic categories are upregulated in WD3 while genes related to storage protein synthesis are downregulated

Next the WT and WD3 transcriptome data for cultured embryos were compared by differential expression (DE) analysis. Among 19,765 genes with detectable gene expression, 1,938 genes were found to be up-regulated in WD3 and 1,465 were down-regulated (Supplementary Table S5). To validate the DE analysis, 7 transcripts that were found to be up-regulated were re-analyzed by quantitative real-time reverse transcription PCR (Supplementary Figure S5). The correlation coefficient between the fold changes obtained by RNA-seq analysis and qRT-PCR was 0.99, showing that both methods agree well (Supplementary Figure S5). Among the validated genes are the two overexpressed ones, *TaWRI1* and *TaDGAT1*, which were found to be up-regulated in WD3 by about 20 and 50-fold, respectively (Supplementary Figure S5).

To functionally categorize pennycress DE genes, we performed over-representation analysis using the Mercator4 v4.6 annotation and enrichment tool (Schwacke et al., 2019). All results for over- and underrepresented gene sets with corrected p-value < 0.05 are listed in detail in Supplementary Table S6. Figure 3 highlights overrepresented gene sets up to the third sublevel of the MapMan4 gene classification system. Among genes upregulated in WD3, genes in top-level categories photosynthesis, carbohydrate metabolism, amino acid metabolism, lipid metabolism, and redox homeostasis were overrepresented (Figure 3). Within photosynthesis (bin 1), 26 genes in the "photosystem II" subcategory and 17 genes in the "Calvin cycle" subcategory—including RubisCO subunits, *RUBISCO ACTIVASE* (*RCA*), and *PHOSPHORIBULOKINASE* (*PRK*)—were upregulated (Supplementary Table S6), indicating that activities of photosynthetic light reactions and the RubisCO shunt are enhanced in WD3. Within lipid metabolism (bin 5), enrichment was observed for genes related to "acetyl-CoA generation", "acetyl-CoA carboxylation" and the "plastidial fatty acid synthase (ptFAS) system," pointing to increased plastidic FAS, in line with the higher lipid content in WD3 embryos (Figure 2). Besides, within the lipid metabolism category sterol biosynthetic genes are overrepresented as well (Figure 3). Downregulated DE genes were dominated by categories linked to protein biosynthesis (bin 17) as well as a few genes related to "protein storage" (bin 19.5) (Figure 3). 155 genes of subcategory 17. 1 "ribosomal biogenesis" were downregulated and among these, many encode for ribosomal subunits (Figure 3). Another highly enriched set of 13 downregulated genes falls under the category of "protein storage" (bin 19.5, Figure 3). This pattern suggests a broad reduction in protein synthesis capacity and storage protein synthesis, consistent with the measured decrease in total protein content in WD3 (Figure 2). Transcripts of seed storage proteins, normally among the most highly expressed transcripts in WT, were markedly reduced. Direct inspection of RNA-seq counts showed that "2S albumin seed storage proteins" (bin 19.5.1.1, 5 genes) and "globulin-type seed storage proteins" (bin 19.5.1.3.1, 8 genes) together accounted for 25.1 ± 0.7% of total reads in WT but only 11.3 ± 0.9% in WD3, representing a two-fold reduction (Supplementary Table S7).

Numerous WRI1 gene targets are up-regulated in WD3

Since the *WRI1* expression level is about 20 times higher in WD3 than in WT (Supplementary Figure S5), WRI1 gene targets are expected to be among the up-regulated ones. During seed development, genes associated with the lower section of the glycolysis pathway and FAS have been shown to be controlled by

WRI1 (Focks and Benning, 1998; Baud et al., 2007; Baud et al., 2009; Maeo et al., 2009; To et al., 2012; Fukuda et al., 2013; Kim et al., 2016; Kuczynski et al., 2022). Examples for genes that were thoroughly characterized as WRI1 gene targets in Arabidopsis are the *Biotin Carboxyl Carrier Protein 2* (*BCCP2*) and the *PLASTIDIC PYRUVATE KINASE BETA SUBUNIT 1* (*PKp-β$_1$*) (Baud et al., 2007; Baud et al., 2009; Maeo et al., 2009; To et al., 2012; Fukuda et al., 2013; Kim et al., 2016). The respective homologs of these in pennycress (TAV2_LOCUS20166, TAV2_LOCUS21171) were found to be about 10 and three-fold up-regulated in WD3, respectively (Supplementary Figure S5) (Supplementary Table S5). We next searched for pennycress homologs of a curated set of WRI1 gene targets in Arabidopsis. Based on a previous study in which WRI1 gene targets were characterized based on in vitro binding activity and phylogenetic conservation of upstream WRI1 binding motifs (Kuczynski et al., 2022), we defined a set of 29 genes as high-confidence WRI1 targets in Arabidopsis and identified 29 pennycress gene homologs (Supplementary Table S8). In all cases we could find WRI1 binding sites in the Arabidopsis genomic upstream regions to be well conserved in the homologous upstream regions in pennycress (Supplementary Table S8). For 27 out of 29 assessed WRI1 targets significant up-regulation was found in cultured WD3 embryos (Supplementary Table S8), which is 9.8 times higher than expected by random chance (hypergeometric p-value 1.9E-20). Since the 29 WRI1 gene targets in our gene set overlap analysis were not identified by a genome-wide approach, we performed a complementary analysis using a set of 401 genes previously identified as direct WRI1 targets in Arabidopsis based on transcriptome analysis of an Atwri1 mutant and WRI1-overexpressing lines (Jo et al., 2024). For 154 of the 401 assessed gene targets, homologs in pennycress were found to be up-regulated in WD3, which is 5.7 times higher than expected by random chance (hypergeometric p-value 5.9E-76). We conclude that pennycress homologs of known WRI1 gene targets in Arabidopsis are upregulated in the WD3 line.

In further assessing the effect of the overexpression of the transcription factor *WRI1* we tested how many genes associated to de-novo FAS and TAG biosynthesis are upregulated (Supplementary Table S9). 32 out of 37 genes coding for enzymes in plastidic FAS listed in Supplementary Table S9 were upregulated, which is 7.1 times higher than expected by random chance (hypergeometric p-value 1.7E-17). In Addition to *DGAT1*, which was overexpressed, several genes encoding for enzymes along the Kennedy pathway (Kennedy, 1961) were upregulated in WD3. In particular, homologs of *LONG-CHAIN ACYL-COA SYNTHASE 1* (TAV2_LOCUS14125), *LYSOPHOSPHATIDIC ACID ACYLTRANSFERASE 2* (TAV2_LOCUS17582), *PHOSPHATIDIC ACID PHOSPHOHYDROLASE 1* (TAV2_LOCUS11638), *DGAT2* (TAV2_LOCUS16550) and *DGAT3* (TAV2_LOCUS3852) were upregulated in WD3 (Supplementary Table S9). In addition, a homolog of *REDUCED OLEATE DESATURATION 1* (TAV2_LOCUS10154), which encodes for phosphatidylcholine:diacylglycerol cholinephosphotransferase (PDCT) (Lu et al., 2009) was upregulated in WD3 (Supplementary Table S9).

Altogether, the upregulation of lipid biosynthesis pathways and the downregulation of ribosomal components and storage protein genes observed in WD3 were identified as important transcriptional motifs associated with the observed lipid / protein tradeoff.

Metabolomic analysis reveals widespread metabolic perturbations by overexpression of *WRI1* and *DGAT1*

In parallel with the transcriptome analysis, untargeted metabolomics was performed on WT and WD3 embryos cultured for 10 days. A total of 127 metabolic intermediates and other polar compounds were identified with high confidence (Supplementary Table S10). Among these, 48 compounds showed significant abundance differences (≥1.5-fold, adjusted $p \leq 0.05$; Table 1), with 29 increased in WD3 and 19 higher in WT (Supplementary Table S10). Table 1 shows the results of pathway enrichment analysis for the 48 significantly altered compounds, indicating that key central carbon metabolism processes such as

the tricarboxylic acid (TCA) cycle, the Calvin cycle as well as amino acid and pyruvate metabolism were strongly affected by overexpression of *WRI1* and *DGAT1*.

Complementary to the untargeted metabolomics, targeted metabolite quantification by LC-MS (Supplementary Table S11) further resolved differences in amino acid, organic acid, sugar, and sugar phosphate pools (Figure 4). The combined analysis shows that the levels of many proteinogenic amino acids changed significantly. Pyruvate-derived (Ala, Leu, Val) and oxaloacetate-derived amino acids (Asn, Asp, Cys, Ile, Lys, Thr) were elevated in WD3, whereas Pro and Phe accumulated to higher levels in WT (Figure 4). Several TCA cycle intermediates were also altered: malate, 2-ketoglutarate (KG), and fumarate (Fum) were increased in WD3, while succinate was more abundant in WT (Figure 4). In glycolysis, WD3 showed increases in glucose 6-phosphate, fructose 6-phosphate, phosphoenolpyruvate, and pyruvate, while fructose 1,6-bisphosphate decreased (Figure 4). Taken together, the changes in the levels of glycolytic intermediates, TCA cycle metabolites, and amino acids in WD3 supports a model for the underlying reprogramming of central metabolism. The observed lipid-protein tradeoff (Figure 2) suggests that glycolytic flux into lipid synthesis is increased in WD3 while flux of amino acids into storage protein synthesis decreased. The reallocation might be driven by increased enzyme activity at the top of glycolysis, which explains increasing the levels of glycolytic intermediates, coupled with a downstream limitation in protein synthesis, leading to the accumulation of both TCA intermediates and free amino acids. The latter is consistent with the observed downregulation of transcripts encoding ribosomal components and storage proteins.

Reorganization of central carbon metabolism between WD3 and WT is revealed by parallel labeling experiments

To further assess how the lipid-protein tradeoff relates to central metabolism, we performed ^{13}C-MFA using three complementary tracer experiments. 95% flux confidence intervals were determined by propagating experimental uncertainty in both flux measurements (Supplementary Table S12) and labeling data (Supplementary Table S13) through a Monte Carlo approach. In some instances, the confidence intervals were validated independently using the parameter continuation method of Antoniewicz *et al.* (Antoniewicz et al., 2006) (Table 2). In addition to ^{13}C-labeled glucose as a tracer, the complementary labeling experiments with two differently labeled forms of alanine proved essential for achieving high-precision flux estimates. For example, resolving flux between cytosolic and plastidic pyruvate kinase (vPK_c, vPK_p) relied on the [2,3-$^{13}C_2$]Ala labeling experiment. This can be demonstrated by repeating the flux estimation while omitting the [2,3-$^{13}C_2$]Ala dataset. In this case the 95% confidence interval for vPK_c increased by roughly an order of magnitude (Supplementary Figure S6A) and the confidence intervals for vPK_c and vPK_p overlap (Supplementary Figure S6B). Likewise, the [1-^{13}C]Ala tracer was critical for resolving fluxes among the network of carboxylation and decarboxylation reactions. This is because much of the [1-^{13}C]Ala is converted to [1-^{13}C]pyruvate and subsequently to $^{13}CO_2$ by the highly active plastidic pyruvate dehydrogenase complex (Schwender et al., 2004). Internal labeled CO_2, in turn, will function as a tracer to track the metabolic fate of carboxylation products. At the same time, ^{13}C label in internal CO_2 will be reduced if low-level labeled intermediates are decarboxylated. Consistent with this role, removing the [1-^{13}C]Ala experiment led to a ~3-fold increase in the confidence interval for RubisCO flux and up to a 10-fold increase in the confidence interval for plastidic glucose-6-phosphate dehydrogenase ($G6PDH_p$) (Supplementary Figure S6A).

Comparison of fluxes between genotypes revealed significant differences (non-overlapping 95% confidence intervals): for 96 comparisons of net fluxes, 11 were higher in WD3 and 27 higher in WT (Supplementary Table S14). The results are summarized in Figure 5 where the flux distribution in central metabolism is shown for WD3 embryos. Accompanying Figure 5, Figure 6 allows a comparison of flux confidence intervals between WT and WD3. Because fluxes through parallel cytosolic and plastidic upper glycolysis could not be unambiguously resolved (Supplementary Figure S7), these were merged into an

uncompartmentalized view based on calculating aggregated flux metrics (See Methods). Overall, WD3 exhibited increased flux into TAG biosynthesis and decreased flux into amino acid accumulation (Figure 5), consistent with the lipid–protein tradeoff observed in biomass composition. Notably, the rise in lipid accumulation in WD3 was associated with an increase in flux through the RubisCO shunt and redistribution of flux in downstream metabolism between phosphoenolpyruvate (PEP) and pyruvate (Figures 5 and 6), which is examined in detail below.

The oxidative pentose phosphate pathway has low activity and contributes at best about 30% of the NADPH demands of fatty acid biosynthesis

During oil synthesis in developing seeds, the Oxidative Pentose Phosphate Pathway (OPPP) is often regarded as the principal source of NADPH for FAS (Rawsthorne, 2002). In WD3, the combined flux through cytosolic and plastidic glucose 6-phosphate dehydrogenase ($vG6PDH_{c+p}$) is relatively small when compared to the flux of pyruvate towards FAS (vPDHp, Figure 5). This suggests that the OPPP has low activity. Comparing the NADPH formation by the OPPP to the fatty acid biosynthesis demands reveals that the OPPP contributes 0% and 6.7% of the NADPH demands for WT and WD3, respectively (Best fit value, Table 2). The best fit value for WD3 is higher, but not significantly so. Based on the two independent methods for statistical confidence (95% confidence interval) for this flux metric, the OPPP contribution ranges between 0% and at most 21% and 27%, respectively (Table 2).

Flux through the RubisCO shunt is increased in WD3

Tracing carbon conversion from glucose to TAG in WD3 reveals that most 3-phosphoglycerate (PGA) is generated through RubisCO, meaning that glycolytic formation of PGA from triose phosphate (TP) via GAPDH ($vGAPDH_{c+p}$) is mostly bypassed by the RubisCO shunt (Figure 5) (Schwender et al., 2004). In WD3, flux through the non-oxidative branch of the pentose phosphate pathway—specifically $vTK1_p$ and $vPPiso_p$—is significantly increased (Figure 5). Correspondingly, PRK and RubisCO fluxes are elevated by 59%, and the significance of this increase is strongly supported by the two independent methods for estimating confidence intervals (Table 2). Consistent with elevated RubisCO shunt activity, transcript levels of transketolase (TK), PRK, multiple RubisCO subunits, and RCA are all increased in WD3 (Figure 5). Many of these genes also fall within the Mercator4 “Calvin cycle” category, of which 17 associated genes are upregulated in WD3 (Figure 3, Supplementary Table S6). Downstream of RubisCO, flux from PGA to PEP ($vPGM_{c+p}$) is also increased by 25% (Figure 5). Together with the above findings on low OPPP activity, these changes indicate that the formation of Ribulose 5-phosphate (RuP_p) in WD3 occurs predominantly through the non-oxidative mode of the RubisCO shunt, rather than through the oxidative mode (Schwender et al., 2004) that would rely on oxidation of hexose phosphate (HP) to RuP_p (Figure 5). Operation of the non-oxidative RubisCO shunt to increase lipid synthesis in WD3 also means that more energy cofactors are required (Schwender et al., 2004). Increased contributions of energy cofactors (ATP, NADPH) from photosynthesis are implied by the strong upregulation of 46 genes in the “Photophosphorylation” category (Figure 3).

Flux through the cytosolic pyruvate kinase is increased in WD3

While, as stated above, upper glycolysis flux cannot be resolved into its cytosolic and plastidic components, from phosphoenolpyruvate (PEP) onward, the flux map in Figure 5 distinguishes cytosolic and plastidic pyruvate kinase activity (Supplementary Figure S6B). In WD3, flux through cytosolic pyruvate kinase (vPK_c) and the subsequent import of pyruvate into the plastid ($vPyr_{c/p}$) increase by 81% and 64%, respectively (Figure 5). The increase in flux from PEP into the lipid precursor pyruvate (Pyr_p) in WD3 comes via the cytosolic route rather than the parallel plastidic pyruvate kinase reaction (vPK_p) (Figure 5).

Malic enzyme contributes little to FAS in both WT and WD3

In addition to vPK_p, plastidic NADPH-malic enzyme may contribute pyruvate and NADPH to FAS in the plastid, in a metabolic reaction sequence called the malate shunt (Smith et al., 1992). In both genotypes, the combined cytosolic and plastidic malic enzyme flux (vME_{c+p}) is marginal relative to the flux through plastidic pyruvate dehydrogenase ($vPDH_p$) (Figure 5, Figure 6). Based on statistical 95% confidence intervals, the amount of NADPH that malic enzyme contributes to FAS biosynthesis is at maximum of about 7% and 2% of the requirement for WT and WD3, respectively (Table 2). Therefore, the malate shunt contributes very little to FAS in pennycress embryos. This contrasts with a previous study on cultured pennycress embryos, which estimated that 17% of the pyruvate entering FAS was derived from malic enzyme activity (Tsogtbaatar et al., 2020). A likely explanation for this discrepancy lies in the nitrogen source used: the other study supplied Gln as the sole nitrogen source, whereas we provided both Gln and alanine (Ala). As seen in Figure 5, Gln and Ala are supplied as a nitrogen source and a substantial fraction of the Gln carbon skeletons is directed into the TCA cycle. In turn, an equivalent molar amount of malate can be removed from the TCA cycle to serve biosynthetic purposes, specifically providing pyruvate via malic enzyme (Mukherjee et al., 2024). When, as being the case in the other study, Gln alone satisfies the nitrogen demand, the anaplerotic flux of C_5 skeletons into the TCA cycle and extraction of malate from it can be larger, potentially providing more pyruvate via malic enzyme.

The increase in lipid biosynthetic flux in WD3 does not apply to the cytosolic elongation process

Tracing carbon flow from pyruvate into TAG reveals a 31% increase in flux through plastidic pyruvate dehydrogenase ($vPDH_p$) in WD3 (Figure 5), consistent with the elevated lipid content of these embryos (Figure 2A). In contrast, flux through cytosolic elongation of long-chain fatty acids (C18) to very-long-chain fatty acids (VLCFAs) ($vFAE_c$) did not change significantly (Figure 5). This finding is most clearly reflected in the reduced FAER observed in WD3, indicating a relative constraint on C18-to-VLCFA elongation capacity (Figure 2B). Consequently, the substantial increase in de novo fatty acid synthesis within plastids, combined with largely unchanged elongation flux, is fully consistent with the fatty acid profiles shown in Figure 2B. Notably, the increased abundance of C20:1 (Figure 2B) despite this apparent limitation cannot be explained by the current flux model, which treats lipid biosynthesis as an aggregated process and does not resolve individual lipid pools or specific enzymatic steps involved in fatty acid modification.

Decreased protein biosynthesis in WD3 coincides with flux reorganization around the TCA cycle

In contrast to the flux increases, 24 flux rates were significantly decreased in WD3 relative to WT (Supplementary Table S14). Seventeen of these relate to the biosynthesis of amino acids and their accumulation in biomass (Supplementary Table S14) and Figure 5 aggregates these into 5 fluxes according to biosynthetic amino acid families. This reduction in flux is in line with the substantial decrease in protein content (Figure 2) and the reduced gene expression related to protein synthesis (Figure 3). Also, in line with the expected overall reduced nitrogen demand in WD3, the uptake of Gln from the medium decreased by 25 % (Figure 5). Since a significant fraction of Gln carbon skeletons enter the TCA cycle, it is not surprising that the flux between KG and citrate (Cit) around the TCA cycle is significantly reduced in WD3 (vKDH, vFM, vCS, Figure 5). Interestingly, these changes in TCA cycle-related fluxes are accompanied by changes in the concentrations of the TCA cycle intermediates KG, succinate (Succ), Fum, and malate (Mal)(Figure 5). Also, attenuation in TCA cycle activity between KG and Cit might cause a decrease in supply of cytosolic acetyl-CoA ($AcCoA_c$, Figure 5), possibly contributing to the above-mentioned limitation in elongation of FA to VLCFAs.

Pennycress embryos grow with high Carbon Conversion Efficiency

In addition to resolving intracellular fluxes, the ^{13}C-MFA–derived flux maps also specify the embryo's overall carbon balance by quantifying model-predicted uptake rates of glucose, Ala, and Gln from the medium, as well as CO_2 efflux to the environment (Figure 5). Assuming these fluxes capture all exchanges between the embryo and its environment, the total carbon balance—commonly expressed as the Carbon Conversion Efficiency (CCE) (Goffman et al., 2005)—can be directly calculated from these flux estimates. Based on this analysis, WT and WD3 embryos retain 85.0 ± 0.6% and 85.0 ± 0.7% of the carbon taken up as glucose, Ala, and Gln, respectively, in biomass (Supplementary Table S14). These values fall within the range reported for other green oilseed systems. *Brassica napus* embryos grown under identical culture conditions exhibit CCE values between 79% and 86% (Schwender et al., 2004; Goffman et al., 2005; Schwender et al., 2015). Reported CCEs include 75% for *Physaria fendleri* (Cocuron and Alonso, 2024) and 82% for soybean embryos (Allen et al., 2009). Only when *Brassica napus* embryos were cultured in the dark, or in one study with embryos of *Camelina sativa*, were substantially lower CCE values of 60% and 32%, respectively, observed (Goffman et al., 2005; Carey et al., 2020). Also, for cultured non-green embryos of maize and sunflower CCE values of 60 % and 50 %, respectively, have been found (Alonso et al., 2007; Cocuron et al., 2019). Specifically for pennycress embryos cultured under similar low-light conditions, a CCE of 93% has been reported (Tsogtbaatar et al., 2020). Overall, the close to 85% CCE observed in this study for both genotypes agrees with the carbon efficient functioning of the RubisCO shunt (Figure 5). Substantially increased FAS in WD3 generates more CO_2 at the pyruvate dehydrogenase step ($vPDH_p$, Figure 5) and most of this increase is reassimilated by increased RubisCO activity. Supplemental Figure S11 illustrates this by providing an overview of all CO_2-producing and CO_2-consuming rates in the network.

As an independent assessment of the medium substrate uptakes and CCE, we measured the depletion of glucose, Gln and Ala from the liquid culture medium along with the amount of carbon accumulated in dry mass by the growing embryos (see methods; Supplementary Table S19). As can be seen in Supplemental Figure S12, the uptakes of glucose, Gln and Ala per gram dry matter formed from the experimental determination are similar to the model predicted fluxes. In addition to the medium substrate depletion, the carbon content in embryo was determined by CHN-elemental analysis of dry mass (Supplementary Table S15). From these empirical measurements, CCE was estimated at 82.8 ± 9.1 % for WT and 80.7 ± 8.0 % for WD3. Although these values are slightly lower than those derived from ^{13}C-MFA, their confidence intervals overlap, and the difference cannot be considered statistically meaningful. Taken together, both flux-based and independently measured CCE estimates support the conclusion that pennycress embryos exhibit highly carbon-efficient growth, consistent with a functioning RubisCO shunt that effectively recaptures internally generated CO_2.

Discussion

In this study, we generated and characterized pennycress lines with seed-specific overexpression of *TaWRI1* and *TaDGAT1* to investigate the metabolic basis of enhanced oil accumulation. Prior studies in other species involving overexpression of *WRI1* alone or in combination with additional factors, have primarily focused on key phenotypic outputs such as oil content or quality (fatty acid composition). Here, we are employing a combination of ^{13}C-MFA, metabolomics, and transcriptomics in cultured embryos to dissect the molecular and biochemical consequences of WRI1 and DGAT1 overexpression in pennycress. The application of ^{13}C-MFA necessitates in vitro cultivation of developing embryos, which imposes physiological conditions that may not fully recapitulate those experienced in planta. However, embryo culture systems have been established for several cruciferous species, including pennycress, that closely approximate the liquid endosperm environment encountered during seed development (Sagun et al., 2023). While this experimental framework captures only a subset of the full developmental program, it enables steady-state flux analysis under controlled conditions, and the metabolic insights obtained are

therefore expected to be at least partially transferable to in planta seed filling. In the cultured embryos, higher lipid and TAG levels were accompanied by a significant reduction in protein content (Figure 2), which allowed us to examine how carbon and nitrogen resources are reallocated. This lipid–protein tradeoff was further reflected in widespread changes in transcript abundance, metabolite pools, and flux distributions across central metabolism, providing new insight into how carbon partitioning is orchestrated during seed oil accumulation.

A dual regulatory mechanism orchestrates carbon partitioning

Coexpression of *WRI1* and *DGAT1* pursues the strategy of maximizing carbon flux into TAG by jointly upregulating sugar catabolism, FAS and TAG assembly (Vanhercke et al., 2013; Napier et al., 2014; Xu and Shanklin, 2016). In light of metabolic control theory—which emphasizes that large changes in pathway flux are rarely achieved through modulation of single enzymatic steps—such coordinated, multi-site regulation represents a particularly promising engineering strategy (Weselake et al., 2024). Indeed, our transcriptome profiling revealed a concerted upregulation of genes involved in glycolysis, fatty acid biosynthesis, and TAG assembly, consistent with enhanced pathway flux that can outcompete other biosynthetic routes (Schwender and Hay, 2012). This shift provides a plausible explanation for the observed lipid–protein tradeoff, whereby increased carbon flux into oil comes at the expense of protein reserves. In addition to upregulation of the sugar to lipid conversion pathway, the strong downregulation of ribosomal components and storage protein transcripts, as well as the increase in the levels of several amino acids, suggests that protein accumulation was actively repressed at the level of ribosome-mediated synthesis, reinforcing the shift toward oil production. Together, these findings reveal that enhanced oil accumulation in pennycress embryos results from both upregulation of TAG synthesis and active transcriptional suppression of protein biosynthesis, underscoring a dual regulatory mechanism that orchestrates carbon partitioning in the embryos. What brought about the transcriptional suppression of protein biosynthesis is unclear as of now. It is also unclear how much the dual regulatory mechanism plays a role in planta given that mature WD3 seeds did not exhibit a significant reduction in storage protein and, likewise, did not display the same magnitude of increase in total lipids (Figure 1). One possible reason why mature WD3 seeds do not show a significant decline in storage protein is that the seed filling process may be distinctly biphasic, like in Arabidopsis, where oil synthesis peaks in the middle phase, while protein accumulation lasts longer (Kanai et al., 2016). In case of pennycress, as stated above, transcriptome time-series data from developing seeds (Claver et al., 2024) show that the expression profile of our cultured embryos most closely resembles the earliest sampled stage (12 DAF, green seeds; Supplementary Figure S4A). Later in planta stages are marked by a pronounced rise in storage-protein transcripts around 20–30 DAF, when expression of WRI1-associated fatty-acid biosynthesis genes has already declined (Supplementary Figure S4B, C).

Photosynthesis and flux redistribution

In WD3 embryos, upregulation of photosynthetic genes (Figure 3) could provide increased production of ATP and NADPH, providing additional energy and reducing power for biosynthesis. This contribution is likely substantial, since our flux analysis shows that generic NADPH-generating pathways in oil biosynthesis, such as the OPPP and the malate shunt, operate at low activity. Notably, we also observed upregulation of the non-oxidative RubisCO shunt (Schwender et al., 2004) in WD3. Because this pathway requires an external supply of reducing equivalents, the increased photosynthetic generation of ATP and NADPH in WD3 would facilitate greater carbon flux through the RubisCO shunt, consistent with the measured flux changes (Figure 5). Thus, induction of photosynthesis in developing seeds, together with enhanced RubisCO shunt activity, represents an additional dimension of metabolic reprogramming under *WRI1*/*DGAT1* overexpression. While WRI1 is a seed specific transcription factor known for upregulating

genes in glycolysis and FAS (Kuczynski et al., 2022) there are no indications for a direct upregulation of photosynthesis by WRI1. However, we observed a striking 190-fold upregulation of TAV2_LOCUS515, a pennycress homolog for *LEAFY COTYLEDON 1* (*LEC1*) in WD3 (Supplementary Table S5). LEC1 is a transcriptional regulator and in Arabidopsis it is known to upregulate photosynthesis genes during early seed development (Pelletier et al., 2017). Therefore, LEC1 could be responsible for upregulation of photosynthesis genes in WD3. In line with this possibility, our analysis of the developmental transcriptome time series of pennycress seeds by Claver *et al.* (Claver et al., 2024) shows that the expression of *LEC1* is highest in the first analyzed stage at 12 DAF, which is characterized as 'green', and decreases significantly as the seeds develop into subsequent stages, which are characterized by a reduction in green color (Supplementary Figure S4B). In addition, LEC1 itself might be directly upregulated by WRI1 since in Arabidopsis and soybean LEC1 itself has been implicated as a potential target of WRI1 (Kuczynski et al., 2022; Jo et al., 2024). This possibility requires further investigation.

Similar to this study, substantial RubisCO shunt activity has been demonstrated previously by isotope tracer experiments in developing green embryos of *Brassica napus* (Schwender et al., 2004; Schwender et al., 2015), *Arabidopsis* (Lonien and Schwender, 2009), pennycress (Tsogtbaatar et al., 2020), and *Physaria* (Cocuron and Alonso, 2024). Complementing this tracer-based evidence, recent genetic data show that disruption of the RubisCO shunt through loss of *PRK* in *Arabidopsis* greatly reduces seed oil accumulation (Deslandes-Herold et al., 2023). Together, these findings suggest that the RubisCO shunt is an integral component of oil biosynthesis in green oilseed embryos across Brassicaceae species.

Upregulation of glycolytic flux through cytosolic pyruvate kinase and enolase is unexplained

Glycolysis operates in both the cytosol and plastid, where parallel isoforms of the pathway coexist. In both WT and WD3 embryos, more than 50% of the total glycolytic flux passes through plastidic pyruvate kinase (PK_p). However, the increase in lower glycolysis observed in WD3 occurred primarily in the cytosolic branch, while PK_p flux remained largely unchanged (Figure 5). This finding is unexpected, since PK_p has been considered the predominant source of pyruvate in developing oilseeds and is thought to be strongly regulated by WRI1. Two main observations have shaped this view: (i) mutations in Arabidopsis genes encoding for PK_p subunits cause substantial reductions in seed oil (Andre et al., 2007; Baud et al., 2008; Lonien and Schwender, 2009), and (ii) genes encoding PK_p isoforms, unlike cytosolic PK (PK_c), are well established as direct WRI1 targets (Ruuska et al., 2002; Baud et al., 2007; Maeo et al., 2009; Kuczynski et al., 2022). Consistent with this, transcripts for all three pennycress PK_p subunits were significantly upregulated in WD3 (genes associated to vPK_p in Figure 5). Nevertheless, transcriptomics revealed a more complex regulatory picture. Of the eight PK_c isoforms, one was upregulated and another downregulated in WD3 (vPK_c in Figure 5). Additional genes associated with lower glycolysis were also induced, including homologs to the Arabidopsis *PHOSPHATE/PHOSPHOENOLPYRUVATE TRANSLOCATOR 1* (TAV2_LOCUS24113), cytosolic *ENOLASE 2* (TAV2_LOCUS12827), and plastidic *ENOLASE 1* (TAV2_LOCUS16328, Supplementary Table S8) (Figure 5). Overall, the general gene regulatory influence on the lower glycolysis flux pattern remains unclear, but it is important to note that flux patterns are also dependent on post-transcriptional control. Both cytosolic and plastidic PK isoforms are subject to extensive allosteric regulation (Plaxton et al., 2002; Andre et al., 2007; Wulfert et al., 2020). In this context, the altered levels of metabolites such as KG and Cit (Figure 4) may modulate in vivo PK activity, potentially overriding transcriptional regulatory inputs and contributing to the unexpected increase in cytosolic PK flux.

Limitations

In this study, we characterized developing in vitro–cultured embryos using a quantitative, multilevel approach that integrated metabolite profiling, transcriptomics, and flux analysis. Importantly, the flux measurements relied on an in vitro embryo culture system, which cannot fully replicate seed development

in planta. As stated above, the in vitro condition corresponds to an early phase of peak expression of FAS genes in seed maturation. Later on, biomass composition is further shaped by late-maturation processes related to desiccation tolerance, dormancy, and seed longevity (Leprince et al., 2017). One late-maturation metabolic aspect that likely significantly influences the lipid content of mature seeds is enhanced lipid turnover late in maturation and during the during the dark period in planta (Koley et al., 2025). Nevertheless, our analysis gives insights into the embryo particularly during the main phase of oil accumulation which should be relevant for the mature seed since, in dry seeds, WD lines exhibited a significant increase in total lipid content relative to the WT (Figure 1).

In addition to the detailed insights into the main phase of seed storage deposition provided by the present study, questions related to additive or synergistic effects of the co-expression of *WRI1* and *DGAT1* could be addressed in future studies. While there are many reports on the effects of overexpression of *WRI1* or *DGAT1* on seed oil in various species (Jako et al., 2001; Cernac and Benning, 2004; Liu et al., 2010; Misra et al., 2013; van Erp et al., 2014; Wu et al., 2014; An and Suh, 2015; Li et al., 2015; Bhattacharya et al., 2016; Ivarson et al., 2016; Roesler et al., 2016; Chen et al., 2018; Guo et al., 2020; Li et al., 2022; Butt et al., 2024; Weselake et al., 2024), reports on the combination of these genes are rare. In a previous study in Arabidopsis, it was reported that seed-specific expression of AtWRI1 or AtDGAT1 increased total fatty acid content in mature seeds by approximately 10 and 6 %, respectively, while in the crossed lines, an increase in fatty acid content of approximately 14% compared to the WT was observed (van Erp et al., 2014). This means that co-expression had the effect of an additional increase over the parent lines.

Suggested further studies and implications for future engineering of oil accumulation

The insights uncovered in this study not only help clarify how WRI1/DGAT1 reprogram central metabolism but also point toward several promising avenues for further enhancing oil accumulation in pennycress.

First, the dual regulatory mechanism we observed—simultaneous upregulation of carbon flux into TAG and transcriptional suppression of protein biosynthesis—suggests that additional gains could be realized by reinforcing or prolonging this early "oil-accumulation phase" in planta. One way to better understand how the lipid/protein tradeoff observed in vitro might be transferred to in planta developing seeds is to characterize transcriptome dynamics and biomass composition in a developmental time series of WT and WD3 seeds. Such a dataset could reveal regulatory transitions that govern the shift from lipid to protein accumulation and thereby inform strategies to delay or attenuate entry into the protein-storage phase, enabling a greater proportion of assimilated carbon to be committed to oil.

Second, flux analysis highlights the non-oxidative RubisCO shunt as a major contributor to fatty-acid–biosynthesis precursor formation. Targeted enhancement of PRK, TK, and RubisCO itself could further elevate activity through this pathway and thereby further increase the FAS rate.

Third, the WD3 flux pattern indicates that plastidic pyruvate supply may remain limiting, as increased lower-glycolysis flux occurred primarily through cytosolic PK rather than PK_p. This finding points toward engineering opportunities to improve plastidic carbon delivery, either by strengthening PK_p activity, modifying its allosteric regulation, or enhancing PEP/pyruvate transport into plastids through carriers such as PPT1 (Tang et al., 2022) or BASS2 (Lee et al., 2017).

Fourth, the malate shunt could be activated. Fluxes through PEP carboxylase (vPEPC) and malic enzyme are low in WT and WD3 embryos (Figures 5) which means that substantially more carbon could be diverted from PEP via oxaloacetate and malate via the malate shunt. Beyond boosting PEP carboxylase, cytosolic NADH-matate dehydrogenase and plastidic malic enzyme, further work is needed to identify malate transport mechanisms across the chloroplast inner envelope. In Arabidopsis, two known malate carriers—the 2-oxoglutarate/malate translocator (DiT1) and the glutamate/malate translocator (DiT2)—mediate only counter-exchange, and thus cannot support net malate import (Weber and Flügge, 2002).

Identification of a dedicated malate transport mechanism in Arabidopsis and other Brassicaceae could therefore be crucial for targeted engineering to activate the malate shunt.

Finally, our data suggests that cytosolic elongation of C18 fatty acids to VLCFAs do not fully scale with increased C18 production in WD3. The reduction in VLCFA proportion in WD3 may represent a metabolic limitation. Modulating *FAE1* or associated elongase complexes, or increasing the supply of cytosolic acetyl-CoA and malonyl-CoA, may alleviate this bottleneck and support further increased TAG formation.

Other research directions relevant to future pennycress oil engineering include strategies to limit lipid turnover during late seed development. Recent findings demonstrate that lipid degradation substantially reduces final seed oil levels in diverse oilseeds (Koley et al., 2025). The steady state ^{13}C-MFA framework applied here does not resolve simultaneous lipid synthesis and degradation. Likewise, analysis of pathway stoichiometries of the carbohydrate to oil conversion in oilseeds indicate that improving the energy/redox balance might be of importance (Schwender, 2025). Development of new isotope tracer approaches to quantify lipid turnover and redox cofactor fluxes could therefore greatly enhance metabolic engineering capabilities.

Materials and methods

Genetic constructs and genetic crosses

cDNAs were generated by reverse transcription of RNA isolated from pennycress Spring32-10 developing seed tissue using an oligo dT primer. PCR products consisting of the *TaWRI1* open reading frame (ORF) and the *TaDGAT* ORF were amplified from these cDNAs using the following primer pairs: TaWRI1_BamHI_Forward: GGGGGATCCGAGTTTAATGAAGAGACC; TaWRI1_NotI_Reverse: GGGGCGGCCGCAATAGATATTCAACCTAG; TaDGAT_EheI_Forward: GGGGGCGCCAATGGCGATTTTGGATTC; TaDGAT_XhoI_Reverse: GGGCTCGAGTTAGCATCGGAACAGATA. Each primer contained a unique restriction site sequence as listed in the primer name. The *TaWRI1* and *TaDGAT1* amplified cDNA sequences are identical to the reverse complement forms of sequences GAKE01001447.1 (positions 131 to 1478) and GAKE01013486.1 (positions 303 to 1913), respectively. The PCR products were restriction enzyme digested at those sites and ligated into digested pENTR2B at those sites. The TaWRI1_pENTR2B clone and the TaDGAT1_pENTR2B clone were then digested with EheI and EcoRV (blunt end cutters) and ligated into the SmaI restriction site (SmaI is also a blunt end cutter) within the pBinGlyRed3 binary vector (Zhang et al., 2013) just downstream of the *Glycine max* glycinin promoter which drives seed-specific expression in plants. These constructs then were stably transformed into pennycress Spring32-10 plants using the *Agrobacterium*-mediated floral dip method described in (McGinn

et al., 2019). Transgenic seedlings were selected based on DsRed fluorescence visualization (McGinn et al., 2019). F_2-generation plants transgenic for the *TaWRI1* seed over-expressing construct (lines W1 and W2) were cross-pollinated with F_2 plants transgenic for the *TaDGAT* seed over-expressing construct (lines D1 and D2) to generate *TaWRI1 TaDGAT* double over-expressing plant lines WD1, WD2, WD3, and WD4. Lines WD1, WD2 and WD4 derive from parents W1 and D1. Line WD3 derives from parents W2 and D2.

PCR screening of transgenic plants

To confirm genetic crosses, genomic DNA was extracted from leaves of WD plants as well as from the untransformed control pennycress plants by the SDS/acetone method (Gouker et al., 2020). PCR screening was performed using a primer pair that is *WRI1* and *DsRed* specific (p844: 5-GGTTGTTGCGACGTTGTTGCGG-3', p76: 5'-TAGTCCTCGTTGTGGGAGGT-3'). In addition, a primer pair that is *DGAT1* and *DsRed* specific was used (p19: 5'-CCGACGCAATCTTCAAACAG-3', p74: 5'-GGGTGCTTCACGTACACCTT-3'). Supplementary Figure S10A and B show maps of the T-DNA region of the *WRI1* and *DGAT1* specific version of the pBinGlyRed3 binary vector along with position of primers used for PCR screening. The primer pairs P844/P76 and P19/P74 can confirm the presence of the genome-integrated T-DNA with parts of the open reading frames of *WRI1* and *DGAT1*, respectively, as shown in Supplementary Figure S10C. In addition, to amplify the full length of the ORFs a primer specific for the glycinin promoter (P937: 5'-CTCAGGTTCTCCGCTTCACAAC-3') was used in combination with the *WRI1* specific P945 (5'- CGGCCGCAATAGATATTCAACCTAG-3') or the *DGAT1* specific P944 (5'-CATCTCGAGTTAGCATCGGAACAGATA-3'). The results of these PCR tests are shown in Supplementary Figure S10D.

Plant growth Conditions

For embryo culture and for seed analysis, pennycress plants were grown in 4-1/2 inch pots in general purpose soil mix (Pro Mix BX, Premier Horticulture Inc., Quakertown, PA) supplemented with Osmocote slow-release fertilizer in a Bio Chambers GR-54 growth chamber (22 °C, 16 h at 400 µmol m^{-2} s^{-1}/18 °C, 8 h dark cycle).

In vitro Embryo Culturing Conditions and isotope tracer experiments

Developing embryos were dissected under sterile conditions from seed pods of WT and WD3 plants at approximately 15 days after flowering. Embryos were transferred to tissue-culture flasks (CytoOne®, CC7682-4875, USA Scientific, Ocala, FL; 10 embryos per flask, n = 4 flasks per labeling condition) containing 30 mL of filter-sterilized growth medium (20% (w/v) polyethylene glycol 4000 (PEG4000), 120 mM glucose, 35 mM Gln, 10 mM Ala, pH 5.8)) and incubated at 20 °C under 50 µmol m^{-2} s^{-1} continuous light for 10 days. Inorganic nutrients were as described before (Schwender et al., 2015). PEG4000 at 20% (w/v) was included to mimic the high osmotic potential of the liquid endosperm surrounding developing embryos in planta, thereby preventing premature germination while allowing continued growth and storage compound accumulation (Schwender and Ohlrogge, 2002; Rolletschek et al., 2021). The three organic substrates (glucose, Gln, Ala) were supplied at concentrations previously optimized for *Brassica napus* embryo culture (Schwender et al., 2015) and used similarly for pennycress embryos (Tsogtbaatar et al., 2020), except that the latter study did not include Ala. As in other cruciferous species, pennycress embryos are photosynthetically active, and the low-light environment within silicles enables embryo plastids to generate NADPH and ATP that support fatty-acid synthesis (Ruuska et al., 2004; Borisjuk et al., 2013). Low-intensity continuous light (10–50 µmol m^{-2} s^{-1}) has been shown to promote or maintain growth of in vitro embryos from *B. napus* (Schwender et al., 2004; Goffman et al., 2005), *A. thaliana* (Lonien and Schwender, 2009), *Camelina sativa* (Carey et al., 2020), *Physaria fendleri* (Cocuron and Alonso, 2024), and pennycress

(Tsogtbaatar et al., 2020). In line with these findings, cultures in this study were maintained under 50 µmol m^{-2} s^{-1} green-filtered continuous light. For labelling experiments, 20% of unlabeled glucose was replaced with the appropriate labelled form (10% [1,2-$^{13}C_2$]-glucose and 10% [U-$^{13}C_6$]-glucose) for glucose labelling experiments. For Ala labelling experiments, unlabeled Ala was replaced with [2,3-$^{13}C_2$]-Ala or [1-^{13}C]-Ala. Before further analysis of biomass compositional analysis and labeling after 10 days of culture, embryos were briefly washed with 0.3 M NaCl to remove residual media. In addition, growth of embryo cultures was monitored by measuring the cross-sectional area in images over 14 days (n=15 per genotype, ImageJ) (Schneider et al., 2012) (Supplementary Table S2).

Transcriptomic Data Analysis

RNA was extracted from cultured embryos using the Spectrum™ Plant Total RNA Kit (Sigma Aldrich), according to the manufacturers protocol. Ten RNAseq libraries (5 per genotype) were prepared and sequenced by Novogene Ltd (www.novogene.uk) on an Illumina HiSeq 4000. The transcriptomic data have been deposited in NCBI's Gene Expression Omnibus (Edgar et al., 2002) and are accessible through GEO Series accession number GSE283815 (https://www.ncbi.nlm.nih.gov/geo/query/acc.cgi?acc=GSE283815). Transcriptomic data was aligned to a reference pennycress genome (Nunn et al., 2022) (GenBank Acc.: GCA_911865555.2) using HISAT2 (2.2.1) (Kim et al., 2019) with default settings. For all samples, at least 96.8% of the raw reads aligned to the genome (Supplementary Table S4). StringTie 2.2.1 (Shumate et al., 2022) was used to assemble reads into transcripts using GenBank Acc.: GCA_911865555.2 as the reference annotation to guide assembly. Novel transcript isoforms were not enabled in the assembly process so that each gene locus is associated with one transcript. Across the 10 sequenced RNA samples, 27,148 transcript levels were quantified, of which 26,392 are associated to gene models in the pennycress reference genome. Read counts were processed by DESeq2 3.17 for differential expression analysis (Supplementary Table S5) (Love et al., 2014). For normalization of read count samples the default method in DESeq2, the median-of-ratios method, was used (Anders and Huber, 2010). Significance calls for differentially expressed genes were made for an adjusted p-value ≤ 5% and for a greater than four-fold change in gene expression or a change of more than 2000 in the mean read count between the genotypes. The genome-predicted pennycress protein sequences (GenBank Acc.: GCA_911865555.2) were mapped onto their closest homologs in Arabidopsis (TAIR10, representative gene models) using Protein-Protein alignment (BLAST ver. 2.2.28 +) (Altschul et al., 1997). Top hits with at least 50% of the query sequence in alignment and at least 40% amino acid identity were kept, which associates 16,971 of the 26,293 pennycress protein sequences with 15,448 unique TAIR identifiers (Supplementary Table S5). Annotation was also achieved by submitting pennycress predicted protein sequences in Mercator4 v4.6 protein function mapping online tool (https://www.plabipd.de/mercator_main.html) (Schwacke et al., 2019), resulting in annotations for 14,568 genes. Based on the Mercator4 annotations, enrichment analysis was performed using the same online tool using the Mercator4 protein categories (BINs). Over- and under-representation was tested using the two-sided Fisher's exact test (5% FDR-adjusted p-value cutoff).

Quantitative reverse transcription real-time PCR (qRT-PCR)

Verification of RNA-Seq results was conducted by qRT-PCR assays for 6 transcripts known to be involved in lipid synthesis. Total RNA from samples was isolated using Qiagen RNeasy Plant Mini Kit for RNA Extraction (Qiagen, Germantown, MD, USA) as described in the manufacturer's user manual. First-strand cDNA was synthesized by using RevertAid First Strand cDNA Synthesis Kit (ThermoFisher, MA, USA). A reference housekeeping gene from Arabidopsis (AT4G12590, ER membrane protein complex subunit-like

protein) was chosen and the corresponded pennycress gene (TAV2_LOCUS21812) was identified by BLAST search against the predicted transcripts. The primers for real-time PCR were designed and synthesized by Integrated DNA Technologies (Coralville, IA, USA). The sequences of primers for reference and target gene are listed in (Supplementary Table S16). Real-time PCR was performed in 96-well plates with a Bio-Rad CFX96 Touch Real-time PCR Detection System. Reactions were in 10- µL volumes containing 2 µL cDNA (0.5 µg/µL), 0.3 µL each primer (10 mM), 2.4 µL water and 5 µL GoTaq® qPCR Master Mix (Promega, Madison, WI, USA). Data were analyzed by CFX Manager™ Software (Bio-Rad, CA, USA). Expression was quantified using the $2^{-\Delta\Delta Ct}$ method (Livak and Schmittgen, 2001). The changes in expression derived from qRT-PCR and RNA-Seq were compared by calculating the Pearson correlation coefficient between the log2 fold-changes using excel.

Biomass Fractionation

The biomass of the harvested embryos was fractionated based on an organic biphasic solvent extraction procedure into a lipid fraction, a polar free metabolites fraction and insoluble cell material (Lonien and Schwender, 2009; Hay et al., 2014). In brief, embryo tissue was homogenized in 3 mL of prechilled methanol:water (4:3, v/v) at 0 °C to 4 °C using an Omni TH Tissue Grinder (Omni International). After a heat step, 3.4 ml of chloroform was added, resulting in a biphasic system that was separated by centrifugation. After the upper methanol/water phase and the lipid phase were removed, the remaining cell pellet was extracted with methanol, and a combined lipid phase was obtained. Finally, the lipid phase, the methanol/water phase and unextractable cell residue (cell pellet) were completely dried and the weights of the fractions were determined. For analysis of dry seeds, the same biphasic solvent extraction was applied, except that seeds were ground by using mortars and pestle under liquid nitrogen.

Starch and protein analysis

To analyze starch content, 2 mg of dry cell pellet was heated to 100°C for 1 hour in 1 mL water. 0.1 mL 50mM acetic acid solution (pH 4.8, adjusted by 10 M NaOH) containing 14 U/mL amyloglucosidase and 63 U/mL alpha-amylase was added and starch was digested at 55°C for 1 hour. The glucose content was then determined using a glucose oxidase assay (MedTest Dx, MI, USA).

Protein content was estimated based on the nitrogen content of the pellet fraction after CHN elemental analysis based on combustion (vario MICRO cube, ELEMENTAR Analysensysteme GmbH, Germany) and after hydrolysis of cell pellet fraction and analysis of the amino acid composition. The factor used to convert %N into % protein, as derived from the amino acid compositional analysis, was 5.92 ± 0.07. Results are listed in Supplementary Table S3b.

Amino acid composition in cell pellet

1 mL water was added to 1 mg cell pellet from the biomass fractionation and heated at 100°C for 1 hour. The supernatant was discharged after 10 minutes of centrifugation. The remaining pellet was washed twice with water and the supernatant was removed after centrifugation. 1 mL 6M HCl was added and the vial was purged with nitrogen before closing with a Teflon/PTFE lined screw cap. After 1 hour at room temperature samples were heated to 110°C for 24 hours. HCl was removed under a constant steam of nitrogen at 80°C. The pellets were redissolved in 0.1% formic acid for LC-MS analysis. The same LC-MS method that applied for the analysis of amino acids and soluble sugars was used (Targeted metabolite analysis). Each amino acid was quantified by its corresponding external standard curve. Tryptophan was lost during protein hydrolysis and adopted data for amino acid composition in pennycress seed meal from literature (Hojilla-Evangelista et al., 2014). Since Asn and Gln were lost as well, the amount of Asp was split 1:1 into Asp and Asn. Glu was split 1:4 into Glu and Gln.

Fatty acid analysis

For analysis of fatty acids by GC/MS, lipids were transesterified by heating to 90 °C in 1 M HCl in methanol for 1 h. After cooling to room temperature, 1 volume of H2O was added, and fatty acid methyl esters were extracted with hexane (Browse et al., 1986). The fatty acid composition was determined by GC-MS (7890A gas chromatograph with 7000 quadrupole mass spectrometer; Agilent Technologies) with a J&W DB 23 capillary column (30 m× 0.25 mm × 0.25 mm) by using scan mode. The injector was held at 250°C and the oven temperature was heated from 80°C to 170°C at 20°C·min^{-1} and from 170°C to 210°C at 5°C·min^{-1}. To quantify the concentration of fatty acids, 100 µg heptadecanoic acid (17:0) was added prior to transmethylation to each sample as an internal standard. Quantification was done by peak area comparison with the internal standard using MSD Chemstation Data Analysis software to integrate GC-MS peak areas (total ion current). Results are listed in Supplementary Table S3f.

For TAG quantification, the lipid extracts were separated by thin-layer chromatography using a 70:30:1 (v/v/v) hexane:diethyl ether:acetic acid solvent system on Silica Gel 60 plates (EMD Millipore). The plates were sprayed with 0.5% primulin in 80:20 (v/v) acetone:water solution to visualize and identify the TAG bands under UV. TAG fractions were identified under UV light, isolated from the plate, and derivatized into FAMEs by incubation in 1 M HCl in methanol. FAMEs were extracted into hexane and dried under an N2 stream prior to resuspending in 100 µL of hexane. The quantification of FAMES was carried out as above.

Analysis of fatty acid profiles

To quantify fatty acid modification patterns, we calculated the fatty acid desaturation ratio (FADR) and fatty acid elongation ratio (FAER), following the approach described by Velasco *et al.* (Velasco et al., 1998). In both ratios, the denominator describes the sum of the molar fractions of the measured unsaturated fatty acid species C*n*:*x*, where *n* = 18, 20, 22 or 24 carbon atoms and *x* = 1, 2, etc. double bonds. For the FADR, the numerator is the sum of molar fractions of polyunsaturated fatty acid species (two or more double bonds, $y \geq 2$):

$$FADR = 100 \times \sum Cn{:}\, y / \sum Cn{:}\, x$$

Similarly, the FAER quantifies the extent of fatty acid chain elongation. Here, the numerator is the sum of molar fractions of unsaturated fatty acids with chain lengths of 20 carbons or longer ($m \geq 20$):

$$FAER = 100 \times \sum Cm{:}\, x / \sum Cn{:}\, x$$

Untargeted metabolite profiling

Freeze-dried embryo samples were extracted according to (Schwender et al., 2015), and the supernatant was used for untargeted profiling of central metabolites. Anionic compounds were analyzed using a Dionex ICS-5000+ HPIC ion chromatography (IC) system (Thermo Fisher Scientific) coupled to a Q Exactive-Plus hybrid quadrupole-orbitrap mass spectrometer (Thermo Fisher Scientific). Amino acids and other cationic metabolites were analyzed using a Vanquish Focused UPLC (Thermo Fisher Scientific) coupled to the same MS system. The non-polar chloroform fraction was subjected to lipidomic analysis as described by (Narvaez-Rivas and Zhang, 2016), using the UPLC-MS system described above. Detailed chromatographic and MS conditions are listed in Supplementary Table S17. Samples were analyzed in randomized order in full MS mode. For compound identification, data-dependent MS/MS analysis was

performed on a pooled probe, which also served as a quality control (QC). Raw data were processed with Compound Discoverer 3.2 software (Thermo Fisher Scientific). A maximum relative standard deviation of 35% in QC peak area was allowed. Compounds were identified using an in-house library, the mzCloud spectral database, and public databases (KEGG, NIST, ChEBI) via mass- or formula-based search algorithms. Group ratios were assessed by ANOVA with Tukey-HSD post hoc testing. Adjusted P-values were calculated using the Benjamini–Hochberg method. Results are provided in Supplementary Table S10. Pathway enrichment analysis was performed using the online available Pathway Analysis module in MetaboAnalyst 6.0 (Pang et al., 2024) (www.metaboanalyst.ca), matching significantly altered metabolites against the KEGG database.

Targeted metabolite analysis

For targeted profiling of 39 free metabolites (Supplementary Table S11), 10-day cultured embryos were extracted using a protocol adapted from (Mata et al., 2016). Briefly, 50 mg fresh weight of embryos were homogenized under liquid nitrogen using a Genogrinder, followed by extraction with 500 µL ice-cold chloroform/methanol (3:7, v/v). Extracts were vortexed, incubated at −20 °C for 2 h, then mixed with 400 µL ice-cold water and incubated at 4 °C for 15 min. Internal standards ($^{13}C_3$-Ala, D_5-Gln, $^{13}C_6$-glucose, and deoxy-glucose-6-phosphate) were added at this step. Following centrifugation (10 min, 14,000 rpm, 4 °C), the aqueous/acetonitrile phase was collected, and the chloroform phase was re-extracted with water. Both aqueous phases were combined and freeze-dried.

Metabolites were analyzed by LC-MS according to (Bajad et al., 2006; Pawlak et al., 2019). A Shimadzu Nexera X2 UHPLC system was coupled to a Sciex QTRAP 4500 triple quadrupole mass spectrometer. Amino acids and soluble sugars were separated using an aminopropyl column (Luna NH2, 100 × 2 mm, 3 µm; Phenomenex). Amino acids were measured in positive ionization mode and sugars in negative ionization mode, using acetonitrile (solvent A) and 20 mM ammonium acetate + 20 mM ammonium hydroxide (solvent B, pH 9.45) with programmed gradients. Organic acids were separated using a Synergi Hydro-RP column (150 × 2 mm, 4 µm; Phenomenex) in negative ionization mode with a formic acid/methanol solvent system. Sugar phosphates were derivatized following (Rende et al., 2019) and separated on a Kinetex EVO C18 column (100 × 2.1 mm, 1.7 µm; Phenomenex) in negative ionization mode.

Quantification was achieved using internal standards: $^{13}C_3$-Ala for amino acids, $^{13}C_6$-glucose for sugars, D_5-Gln for organic acids, and deoxy-glucose-6-phosphate for sugar phosphates. All LC gradients and MS parameters are provided in Supplementary Table S18. Results are reported in Supplementary Table S11.

Medium substrate uptake measurements

In flux modeling, medium substrate uptake rates of the growing embryo (glucose, Ala, Gln) were treated as unknowns estimated by fitting labeling data. To cross-check these predictions, uptake rates were experimentally determined during 10-day embryo culture (Supplementary Table S19). Embryos (n = 15) were grown in 6 mL medium, and substrate depletion was quantified alongside dry weight increase. Measurements followed a stable isotope dilution approach similar to (Shi et al., 2023). After culture, 1 mL sorbitol (0.7 M) was added to the 6 mL culture medium. From this, 100 µL medium was mixed with isotope-labeled standards ($^{13}C_6$-glucose, $^{13}C_6$-sorbitol, D_5-Gln, $^{13}C_3$-Ala) and water. To remove PEG-4000 from the medium, samples were extracted with chloroform and centrifuged (20 min, 3750 rpm, 4 °C). The aqueous phase was analyzed by direct infusion into a Sciex 4500 QTRAP mass spectrometer in MRM mode. Mass spectrometry settings are given in Supplementary Table S20. Substrate concentrations were calculated from isotope ratios (unlabeled vs. labeled standards), and medium volumes were corrected using the sorbitol internal standard.

Biomass composition for ^{13}C-metabolic flux analysis

Biomass fluxes were derived from compositional data (Supplementary Table S3) using a hierarchical calculation scheme that partitions total dry embryo mass into lipids, free metabolites, and cell pellet, and further into subfractions (protein, starch, cell wall polymers, major glycerolipid classes, and major quantified free metabolites). Because lipid classes were not quantified in this study, the distribution of lipid classes was taken from published values for *Brassica napus* seeds (Norton and Harris, 1975). The fatty acid composition of the total lipids fraction was applied to all lipid classes. 20% of the weight of the free metabolites fraction was assumed to be made up from inorganic compounds. Since free metabolites account for ~25% of total embryo dry mass in both genotypes, this corresponds to ~5% ash content, consistent with reported values for *B. napus* seeds (Carré et al., 2016). The full scheme and calculations are summarized in Supplementary Table S3. Statistical uncertainty was assessed by Monte Carlo resampling that repeats the hierarchical calculation scheme 5000 times. This resulted in mean values and standard deviations for 117 biomass components, which were aggregated into 21 biomass fluxes, with variances summed to estimate the uncertainty of each flux (Supplementary Table S12). Fluxes are reported in mmol g^{-1} dry weight and provide the scaling reference for the flux model.

Labeling analysis for ^{13}C-metabolic flux analysis

Analysis of isotope enrichment was done with an Agilent 8890N GC coupled to an Agilent 5977B quadrupole mass spectrometer (Agilent Technologies). As described in detail before (Lonien and Schwender, 2009) fractional labeling information in selected fragments was measured in single ion monitoring mode for the following metabolites (Supplementary Table S13): tert-butyl-dimethylsilyl derivatives of amino acids derived from hydrolysis of cell pellet fraction (23 fragments in 12 amino acids). Glycerol derived from transmethylation of triacylglycerols (lipid fraction) was analyzed as trifluoroacetate derivative (2 fragments). Glucose derived from starch (cell pellet) was analyzed as glucose methoxime penta-acetate (1 fragment). After hydrogenation of the lipid-derived fatty acid methyl esters, saturated fatty acid methyl esters were analyzed (2 fragments in C18 and C20). The fraction of free polar metabolites was derivatized as methoxyamine-trimethylsilyl derivatives, and sucrose-(trimethylsilyl)$_8$ was analyzed (1 fragment).

Mass spectrometry data were extracted from chromatograms using the ChemStation Program (MSD ChemStation; Agilent Technologies) and correction for naturally occurring isotopes (C, H, N, O, S, Si) in the derivative side chains was applied as reported before (Lonien and Schwender, 2009). For each genotype, in total 346 MS measurements were averaged from three independent labeling experiments (Supplementary Table S13). The standard deviation over all modeled mass spectrometry data points was 0.276 % on the isotope enrichment scale. In the flux modeling process, we set the statistical uncertainty of all MS measurements to a uniform value of 0.55% (two times the overall standard deviation), unless the original experimental standard deviation for a mass peak was higher than that. The applied standard deviation is similar to the values used in previous flux studies (Schwender et al., 2006; Schwender et al., 2015). This procedure facilitates passing the statistical goodness-of-fit test but comes at the cost of increased uncertainty in the confidence intervals of the flow results (Schwender et al., 2006).

Metabolic and isotopic steady state condition

In this study, a steady-state ^{13}C-Metabolic Flux Analysis (^{13}C-MFA) approach was employed. The general approach of in vitro–culturing dissected embryos in a medium that mimics the in planta liquid endosperm environment and the use of stable isotope labeled medium substrates to trace pathway usage in central metabolism has been successful for several crucifer species, including *Brassica napus* (Schwender et al., 2006; Schwender et al., 2015), *Arabidopsis thaliana* (Lonien and Schwender, 2009), *Camelina sativa* (Carey et al., 2020), *Physaria fendleri* (Cocuron and Alonso, 2024), and pennycress (Tsogtbaatar et al., 2020).

Accurate flux determination by steady-state MFA requires that both metabolic and isotopic steady states are sufficiently approximated to prevent inaccuracies in flux estimation (Ratcliffe and Shachar-Hill, 2006). As a precondition this requires constant growth conditions. To ensure adequate culture density in order to prevent nutrient depletion, 15 embryos were grown for 10 days in 30 ml liquid growth medium and as described above (see Methods). Quantification of organic substrate consumption in the culture medium (Table S18) revealed that the concentrations of glucose, Ala, and Gln declined by less than 10% over the culture period and therefore remained relatively stable and continuously available. Besides the organic nutrients, we determined that phosphorus can be depleted, but only with culture densities higher than 30 embryos per 30 ml medium. As in previous similar studies, light was supplied continuously, since a day-night rhythm would likely cause diurnal fluctuations in metabolic activity. To further ensure conditions that enable a steady state, embryo growth was monitored in culture. This showed that the cultured embryos were still in an active growth phase after 10 days, the time of their removal, which was reflected in the continued growth of the control group beyond day 10 (Table S2). Altogether, for these parameters we conclude that the conditions exist for near-steady-state conditions with respect to both metabolism and isotopic labeling.

Ideally, the amount of biomass newly synthesized during the labeling experiment should exceed the quantity of initial cellular material present in the culture medium by approximately two orders of magnitude. If this condition is not met, the isotopic dilution by the unlabeled inoculum can be so significant that it leads to inaccuracies in the estimation of the flux parameters. This issue has previously been reported for cultured embryos of *A. thaliana*, where a computational correction procedure was developed to account for the isotopic dilution effect (Lonien and Schwender, 2009). During flux parameter fitting, this correction introduces an additional free parameter representing the contribution of unlabeled inoculum biomass, thereby allowing the model to estimate and compensate for its influence (Lonien and Schwender, 2009). In the present study, model fitting estimated the proportion of unlabeled inoculum biomass to be 2.1 ± 1.0% and 3.9 ± 1.0% of total biomass for the WT and WD3 samples, respectively.

Metabolic Flux Analysis

^{13}C-labeling experiments were performed on WT and WD3 embryos cultured with isotopically labeled carbon substrates (120 mM glucose, 35 mM Gln, and 10 mM Ala) following established protocols (Schwender et al., 2015). Three parallel labeling setups were used: (i) glucose mixture (80% unlabeled, 10% [1,2-^{13}C_2]-glucose, 10% [U-^{13}C_6]-glucose), (ii) Ala labeled at carbons 2 and 3 ([2,3-$^{13}C_2$]-Ala), and (iii) Ala labeled at carbon 1 ([1-^{13}C]-Ala) (Schwender et al., 2006). Labeling signatures from these experiments were integrated to generate a single flux map per genotype.

Mass isotopomer distributions were quantified for 29 molecular fragments from 17 analytes (Supplementary Table S13) and combined with 21 biomass flux measurements (Supplementary Table S12) for flux parameter fitting. The stoichiometric network was based on a previously published *B. napus* model (Schwender et al., 2015) with minor modifications for pennycress (Supplementary Table S21, Supplementary Table S22). Specifically, in addition to the plastidic transaldolase (vTA), the pennycress network includes an alternative route to sedoheptulose-7-phosphate via sedoheptulose-7-phosphate aldolase and sedoheptulose bisphosphatase (vSaldo_p). The final model comprised 127 reactions, of which 36 net fluxes and 25 exchange fluxes were free parameters. These included 21 biomass fluxes, uptake fluxes for glucose, Ala, and Gln (vHex_HPc, vuptAla, vuptGln), and CO_2 efflux (vCO2_out).

Flux estimation was performed using the **Influx_si** toolbox (version 6.1) (Sokol et al., 2012). Input files in FTBL format (http://www.13cflux.net) are provided in Supplementary File 1. Biomass fluxes were scaled so that all net fluxes fell approximately within the [0,1] range. To obtain best-fit solutions,

optimization was initiated with random parameter values drawn from [0,1] ("--irand" option). For both genotypes, repeated optimizations converged to stable χ^2 values: 217.27 for WT and 234.80 for WD3, well within the critical range (200.51–271.76) for 235 degrees of freedom at the 95% confidence level (Long and Antoniewicz, 2019) (Supplementary Table S23).

Flux uncertainty was assessed using a Monte Carlo approach with the command influx_s --irand --sens=mc=1000 <modelname>.ftbl. This procedure repeats the model fitting 1000 times, each time perturbing the ^{13}C-labeling and flux measurement data by pseudo-random noise according to their standard deviations. Ninety-five percent confidence intervals (CIs) were calculated from the resulting distributions using the Microsoft Excel PERCENTILE.INC function. Selected fluxes were additionally validated by a parameter continuation method (Antoniewicz et al., 2006), in which the flux of interest was stepwise displaced from its optimum, followed by repeated fitting until χ^2 consistently increased. The 95% CI boundary was defined as a χ^2 increase of 3.841 (χ^2_95%,1) above the optimum.

Flux estimates and CIs were normalized to 1 g dry weight, reported in relative units of mmol g^{-1} dw (Supplementary Table S14). Fluxes were considered significantly different between genotypes if their 95% CIs did not overlap.

Aggregated flux metrics

Although the flux model includes explicit compartmentalization of cytosolic and plastidic glycolysis (Supplementary Table S14), this level of parallelism is not uniformly resolved. For example, the 95% confidence intervals for cytosolic and plastidic glyceraldehyde-3-phosphate dehydrogenase (GAPDH) fluxes are relatively large (Supplementary Figure S7A), indicating that the experimental data do not provide sufficient information to determine how upper glycolysis is partitioned between the two compartments. A common strategy in ^{13}C-MFA is to iteratively repeat flux fitting while simplifying the model topology to identify the level of detail that can be supported by the data. Here, instead of reducing model complexity prior to flux fitting, we exploited the Monte-Carlo framework to simplify the model after parameter estimation (Shi et al., 2023). As shown in Supplementary Figure S7, summing GAPDHc and GAPDHp fluxes across Monte-Carlo sampled flux vectors yields a combined GAPDH flux with substantially lower statistical uncertainty, and this result matches that obtained by merging the reactions before flux fitting. Beyond merging parallel reactions, Monte-Carlo flux samples also allow convenient calculation of statistical uncertainty for any linear combination of fluxes of interest such as flux sums or flux ratios. For example, in a graphic display of the flux results one might wish to not show all of the amino acid biosynthetic fluxes the model contains but rather aggregate all of the branched-chained amino acids into one (Figure 5). Following this principle, Supplementary Table S14 reports 17 such aggregated flux metrics. Figure 5 displays upper-glycolysis and several additional fluxes in this aggregated form rather than showing the original, more highly resolved flux values.

Statistical analysis

Compositional comparisons were performed using one-way ANOVA with number of biological replicates per condition as indicated in the figure or table legends. Unless stated otherwise, mean values were deemed to be statistically significantly different for $p < 0.05$.

Data availability

The transcriptomic data from this study have been deposited in NCBI's Gene Expression Omnibus (Edgar et al., 2002) and are accessible through GEO Series accession number GSE283815 (https://www.ncbi.nlm.nih.gov/geo/query/acc.cgi?acc=GSE283815).

Accession Numbers

The following genes mentioned in the study can be found in TAIR (https://www.arabidopsis.org/): bile acid:sodium symporter family protein, BASS2 (AT2G26900) ; *BCCP2* (AT5G15530); *DGAT1* (AT2G19450); *DGAT2* (AT3G51520); *DGAT3* (AT1G48300); *ENO1* (AT1G74030); *ENO2* (AT2G36530); FATTY ACID ELONGATION1, FAE1 (AT4G34520); glutamate/malate translocator, DiT2 (AT5G64280); *GOLDEN2-LIKE 2* (AT5G44190); ER membrane protein complex subunit-like protein (AT4G12590); *LEAFY COTYLEDON 1* (AT1G21970); *LONG-CHAIN ACYL-COA SYNTHASE 1* (AT2G47240); *LYSOPHOSPHATIDIC ACID ACYLTRANSFERASE 2* (AT3G57650); 2-oxoglutarate/malate translocator, DiT1 (AT5G12860); *PHOSPHATIDIC ACID PHOSPHOHYDROLASE 1* (AT3G09560); PHOSPHORIBULOKINASE, PRK (AT1G32060); *PKp-β₁* (AT5G52920); *PHOSPHATE/PHOSPHOENOLPYRUVATE TRANSLOCATOR 1, PPT1* (AT5G33320); *REDUCED OLEATE DESATURATION 1* (AT3G15820); *RUBISCO ACTIVASE*, *RCA* (AT2G39730); *WRI1* (AT3G54320).

Author contributions

JSc and JCS conceived the project. JCS, MM and BAJ designed WRI1 and DGAT1 genetic constructs. MM, BAJ, and JCS generated and provided *WRI1*/*DGAT1* transgenic seeds. BG performed RNA extraction for RNAseq analysis. NYHK and JSc performed alignment of RNAseq data to genome. CK, NYHK and HS performed embryo culture and ^{13}C-labeling experiments and compositional analysis. CK and HS grew plants and performed seed compositional analysis. NYHK and HS performed Mass Spectrometry analysis of labeled compounds. JSc and NYHK performed computational flux modeling analysis. HS Performed targeted metabolomics experiments. HR, AH performed untargeted metabolomics experiments. JSc and NYHK analyzed data and drafted manuscript. JSc wrote manuscript with contributions from HR. All authors critically revised and agreed to the published version of the manuscript.

Supplemenatry data

Supplementary Figure S1: Alignment of the deduced amino acid sequences of WRINKLED 1 (WRI1) isoforms from pennycress and *A. thaliana*.

Supplementary Figure S2: Alignment of the deduced amino acid sequences for acyl-CoA:diacylglycerol acyltransferase 1 (DGAT1) in pennycress and *A. thaliana*.

Supplementary Figure S3: Biomass composition of wild type (WT) as well as *WRI1*/*DGAT1* transgenic cultured embryos.

Supplementary Figure S4: Comparison of transcriptome profiles of pennycress WT and WD3 embryos to developing seed stages.

Supplementary Figure S5: Comparison the relative gene expression levels between WD3 and WT cultured embryos.

Supplementary Figure S6: Dependence of flux identifiability on the combination of parallel labeling experiments (WT).

Supplementary Figure S7: Merging cytosolic and plastidic fluxes for glyceraldehyde 3-phosphate dehydrogenase (GAPDH) into one reduces the statistical uncertainty in the flux value.

Supplementary Figure S8: Determination of confidence intervals for RubisCO (A, B) and cytosolic pyruvate kinase flux (C, D).

Supplementary Figure S9: Determination of confidence intervals for the sum of cytosolic and plastidic glucose 6-phosphate dehydrogenase (A, B) and the sum of cytosolic and plastidic malic enzyme (C, D).

Figure S10: Vector constructs and PCR screening method to confirm the genetic cross of WRI1 and DGAT1 overexpressing pennycress lines.

Figure S11: Network wide balance of CO_2 consumption and production in growing WT (blue) and WD3 (red) pennycress embryos.
Figure S12: Uptakes of organic medium substrates by pennycress cultured WT and WD3 embryos.
Supplementary Table S1: Dry seed analysis.
Supplementary Table S2: Growth of embryos in culture.
Supplementary Table S3: Biomass Composition of cultured wild type (WT) and WD3 embryos.
Supplementary Table S4: Summary of RNAseq sequencing data.
Supplementary Table S5: Differential expression analysis data for pennycress cultured embryos.
Supplementary Table S6: Mercator4 protein category (BIN) enrichment analysis of differentially expressed genes in cultured embryos.
Supplementary Table S7: Expression level of seed storage proteins in wild type (WT) and WD3.
Supplementary Table S8: Comparison of 29 Arabidopsis genes that are WRI1 gene targets with high confidence with gene homologs in pennycress.
Supplementary Table S9: Differential expression analysis of genes in plastidic fatty acid and triacylglycerol biosynthesis.
Supplementary Table S10: Untargeted metabolomic analysis.
Supplementary Table S11: Targeted metabolomic analysis of pennycress cultured embryos.
Supplementary Table S12: Flux into biomass.
Supplementary Table S13: Label Measurements for parallel labeling experiments with different ^{13}C-tracers.
Supplementary Table S14: Flux estimates.
Supplementary Table S15: Elemental analysis of cultured embryos.
Supplementary Table S16: Primer sequences for qRT-PCR.
Supplementary Table S17: Chromatographic and Mass spectrometry conditions for untargeted metabolome and lipidome analyses.
Supplementary Table S18: Chromatographic conditions and mass spectrometer parameter settings for targeted analysis of metabolites.
Supplementary Table S19: Measured uptakes of carbon and nitrogen substrates from the medium by cultivated embryos.
Supplementary Table S20: Mass spectrometer parameter settings for analysis of medium substrate levels.
Supplementary Table S21: Reaction network with carbon transitions and mapped pennycress genes.
Supplementary Table S22: Metabolite names.
Supplementary Table S23: Statistical test for goodness of fit.
Supplementary file 1: input files in ftbl format for influx_si flux modeling toolbox.

Conflict of interest

The authors declare no conflict of interest.

Funding

Design of genetic constructs, genetic transformation of plants, genetic crosses, RNA extractions and transcriptome sequencing were performed with support from the National Institute of Food and Agriculture, United States Department of Agriculture, under award number 2018- 67009-27374 to JCS and the United States Department of Energy, Office of Science, Office of Biological and Environmental Research, Genomic Science Program grant no. DE-SC0021286 to JCS. ^{13}C-labeling experiments, compositional analysis, Mass Spectrometry analysis of labeled compounds, computational flux modeling

analysis and targeted metabolomics were performed with support from the United States Department of Energy, Office of Science, Office of Basic Energy Sciences under contract number DE-SC0012704, specifically through the Physical Biosciences program of the Chemical Sciences, Geosciences, and Biosciences Division, to JSc. HR and AH acknowledge funding by the 'Bundesministerium für Bildung und Forschung' (BMBF) in frame of the AVATARS project (grant number 031B 0770B).

Tables

Table 1. KEGG pathway enrichment analysis of significantly altered polar metabolites. Untargeted LC–MS profiling (Supplementary Table S10) identified polar 127 metabolites, of which 48 changed significantly (≥1.5-fold, adjusted $p < 0.05$). Enrichment analysis was performed using MetaboAnalyst 6.0; 41 metabolites mapped to KEGG Arabidopsis pathways. Pathways with FDR < 0.05 are shown; complete results are provided in Supplementary Table S24.

KEGG Pathway Name	Hits	Total	Enrichment ratio	FDR
Citrate cycle (TCA cycle)	5	20	11.9	0.002
Carbon fixation by Calvin cycle	5	21	11.3	0.002
Valine, leucine and isoleucine biosynthesis	5	22	10.8	0.002
Alanine, aspartate and glutamate metabolism	4	22	8.6	0.02
Pyruvate metabolism	4	23	8.2	0.02

Table 2: Determination of statistical confidence limits for selected fluxes by two methods. For all fluxes the limits of the 95% confidence intervals were calculated based on Monte Carlo stochastic simulation. For validation, for the selected fluxes listed here the confidence intervals were determined independently by a parameter continuation method (Antoniewicz et al., 2006) as detailed in Methods. Graphical representations of Monte Carlo and parameter continuation procedures are shown in Supplementary Figure S8 and Supplementary Figure S9. Flux units [mmol / g dw].

genotype	Best fit value	Monte Carlo confidence limits	parameter continuation confidence limits
RubisCO (vRub)			
WT	2.69	[2.08 3.28]	[2.09 3.22]
WD3	4.27	[3.59 5.08]*	[3.56 5.09]*
Cytosolic pyruvate kinase (vPK_c)			
WT	2.33	[2.16 2.72]	[2.1 2.75]
WD3	4.21	[3.99 5.13]*	[3.96 5.21]*
Combined cytosolic and plastidic malic enzyme (vME_c + vME_p)			
WT	0.32	[0.1 0.53]	[0.09 0.6]
WD3	0	[0 0.23]	[0 0.18]
Combined cytosolic and plastidic glucose 6-phosphate dehydrogenase ($vG6PDH_c$ +$vG6PDH_p$)			
WT	0	[0 0.85]	[0 0.29]
WD3	0.35	[0 1.34]	[0 1.42]
% of NADPH demand by malic enzyme (vME_c + vME_p)†			
WT	3.84	[1.22 6.46]	[1.1 7.22]
WD3	0	[0 2.25]	[0 1.7]
% of NADPH demand by OPPP†			
WT	0	[0 21]	[0 7.1]
WD3	6.7	[0 26.6]	[0 27.4]

*, significant difference between WD3 and WT based on non-overlapping confidence intervals. †, % of NADPH demand of fatty acid synthesis that is generated by malic enzyme or OPPP. For details on this calculation see flux mapping equations in Supplementary Table S14.

References

Allen DK (2016) Quantifying plant phenotypes with isotopic labeling & metabolic flux analysis. Curr Opin Biotechnol **37:** 45-52

Allen DK, Ohlrogge JB, Shachar-Hill Y (2009) The role of light in soybean seed filling metabolism. Plant J **58:** 220-234

Alonso AP, Goffman FD, Ohlrogge JB, Shachar-Hill Y (2007) Carbon conversion efficiency and central metabolic fluxes in developing sunflower (*Helianthus annuus* L.) embryos. Plant J **52:** 296-308

Altendorf K, Isbell T, Wyse DL, Anderson JA (2019) Significant variation for seed oil content, fatty acid profile, and seed weight in natural populations of field pennycress (Thlaspi arvense L.). Industrial Crops and Products **129:** 261-268

Altschul SF, Madden TL, Schaffer AA, Zhang J, Zhang Z, Miller W, Lipman DJ (1997) Gapped BLAST and PSI-BLAST: a new generation of protein database search programs. Nucleic Acids Res **25:** 3389-3402

An D, Suh MC (2015) Overexpression of Arabidopsis WRI1 enhanced seed mass and storage oil content in Camelina sativa. Plant Biotechnology Reports **9:** 137-148

Anders S, Huber W (2010) Differential expression analysis for sequence count data. Genome biology **11:** R106

Andre C, Froehlich JE, Moll MR, Benning C (2007) A heteromeric plastidic pyruvate kinase complex involved in seed oil biosynthesis in *Arabidopsis*. The Plant Cell **19:** 2006-2022

Antoniewicz MR, Kelleher JK, Stephanopoulos G (2006) Determination of confidence intervals of metabolic fluxes estimated from stable isotope measurements. Metab Eng **8:** 324-337

Arias CL, Quach T, Huynh T, Nguyen H, Moretti A, Shi Y, Guo M, Rasoul A, Van K, McHale L, Clemente TE, Alonso AP, Zhang C (2022) Expression of AtWRI1 and AtDGAT1 during soybean embryo development influences oil and carbohydrate metabolism. Plant Biotechnol J **20:** 1327-1345

Bajad SU, Lu WY, Kimball EH, Yuan J, Peterson C, Rabinowitz JD (2006) Separation and quantitation of water soluble cellular metabolites by hydrophilic interaction chromatography-tandem mass spectrometry. Journal of Chromatography A **1125:** 76-88

Bates PD, Browse J (2012) The significance of different diacylgycerol synthesis pathways on plant oil composition and bioengineering. Frontiers in Plant Science **3:** 147

Baud S, Dubreucq B, Miquel M, Rochat C, Lepiniec L (2008) Storage reserve accumulation in Arabidopsis: metabolic and developmental control of seed filling. *In* The Arabidopsis Book. American Society of Plant Biologists

Baud S, Mendoza MS, To A, Harscoet E, Lepiniec L, Dubreucq B (2007) WRINKLED1 specifies the regulatory action of LEAFY COTYLEDON2 towards fatty acid metabolism during seed maturation in *Arabidopsis*. Plant J **50:** 825-838

Baud S, Wuilleme S, To A, Rochat C, Lepiniec L (2009) Role of WRINKLED1 in the transcriptional regulation of glycolytic and fatty acid biosynthetic genes in Arabidopsis. The Plant journal **60:** 933-947

Bhattacharya S, Das N, Maiti MK (2016) Cumulative effect of heterologous AtWRI1 gene expression and endogenous BjAGPase gene silencing increases seed lipid content in Indian mustard Brassica juncea. Plant Physiology and Biochemistry **107:** 204-213

Borisjuk L, Neuberger T, Schwender J, Heinzel N, Sunderhaus S, Fuchs J, Hay JO, Tschiersch H, Braun HP, Denolf P, Lambert B, Jakob PM, Rolletschek H (2013) Seed Architecture Shapes Embryo Metabolism in Oilseed Rape. The Plant cell **25:** 1625-1640

Browse J, McCourt PJ, Somerville CR (1986) Fatty acid composition of leaf lipids determined after combined digestion and fatty acid methyl ester formation from fresh tissue. Anal Biochem **152:** 141-145

Butt M, Imran M, Rehman T, Intisar A, Lindsey K, Sarwar G, Qaisar U (2024) Seed-specific expression of AtWRI1 enhanced the yield of cotton seed oil. Scientific Reports **14:** 30750

Carey LM, Clark TJ, Deshpande RR, Cocuron JC, Rustad EK, Shachar-Hill Y (2020) High Flux Through the Oxidative Pentose Phosphate Pathway Lowers Efficiency in Developing Camelina Seeds. Plant Physiol **182:** 493-506

Carré P, Citeau M, Robin G, Estorges M (2016) Hull content and chemical composition of whole seeds, hulls and germs in cultivars of rapeseed (Brassica napus). OCL **23:** A302

Cernac A, Benning C (2004) WRINKLED1 encodes an AP2/EREB domain protein involved in the control of storage compound biosynthesis in *Arabidopsis*. Plant J **40:** 575-585

Chen G, Harwood JL, Lemieux MJ, Stone SJ, Weselake RJ (2022) Acyl-CoA:diacylglycerol acyltransferase: Properties, physiological roles, metabolic engineering and intentional control. Prog Lipid Res **88:** 101181

Chen L, Zheng Y, Dong Z, Meng F, Sun X, Fan X, Zhang Y, Wang M, Wang S (2018) Soybean (Glycine max) WRINKLED1 transcription factor, GmWRI1a, positively regulates seed oil accumulation. Mol Genet Genomics **293:** 401-415

Clark TJ, Guo L, Morgan J, Schwender J (2020) Modeling Plant Metabolism: From Network Reconstruction to Mechanistic Models. Annu Rev Plant Biol **71:** 303-326

Claver A, Lujan MA, Escuin JM, Schilling M, Jouhet J, Saviron M, Lopez MV, Picorel R, Jarne C, Cebolla VL, Alfonso M (2024) Transcriptomic and lipidomic analysis of the differential pathway contribution to the incorporation of erucic acid to triacylglycerol during Pennycress seed maturation. Front Plant Sci **15:** 1386023

Cocuron JC, Alonso AP (2024) 13C-labeling reveals non-conventional pathways providing carbon for hydroxy fatty acid synthesis in Physaria fendleri. J Exp Bot **75:** 1754-1766

Cocuron JC, Koubaa M, Kimmelfield R, Ross Z, Alonso AP (2019) A Combined Metabolomics and Fluxomics Analysis Identifies Steps Limiting Oil Synthesis in Maize Embryos. Plant Physiol **181:** 961-975

Deslandes-Herold G, Zanella M, Solhaug E, Fischer-Stettler M, Sharma M, Buergy L, Herrfurth C, Colinas M, Feussner I, Abt MR, Zeeman SC (2023) The PRK/Rubisco shunt strongly influences Arabidopsis seed metabolism and oil accumulation, affecting more than carbon recycling. Plant Cell **35:** 808-826

Dorn KM, Fankhauser JD, Wyse DL, Marks MD (2013) De novo assembly of the pennycress (Thlaspi arvense) transcriptome provides tools for the development of a winter cover crop and biodiesel feedstock. The Plant journal : for cell and molecular biology **75:** 1028-1038

Dyer JM, Stymne S, Green AG, Carlsson AS (2008) High-value oils from plants. The Plant Journal **54:** 640-655

Edgar R, Domrachev M, Lash AE (2002) Gene Expression Omnibus: NCBI gene expression and hybridization array data repository. Nucleic Acids Res **30:** 207-210

Focks N, Benning C (1998) wrinkled1: A novel, low-seed-oil mutant of *Arabidopsis* with a deficiency in the seed-specific regulation of carbohydrate metabolism. Plant Physiol **118:** 91-101

Fukuda N, Ikawa Y, Aoyagi T, Kozaki A (2013) Expression of the genes coding for plastidic acetyl-CoA carboxylase subunits is regulated by a location-sensitive transcription factor binding site. Plant Mol Biol **82:** 473-483

Gautam B, Kim H, Wang C, Park K, Cahoon EB, Sedbrook JC (2025) Meeting Liquid Biofuel and Bioproduct Goals: Biotechnological Design of the Intermediate Oilseeds Pennycress and Camelina, and Beyond. Journal of Experimental Botany

Goffman FD, Alonso AP, Schwender J, Shachar-Hill Y, Ohlrogge JB (2005) Light enables a very high efficiency of carbon storage in developing embryos of rapeseed. Plant Physiol **138:** 2269-2279

Gouker FE, Guo Y, Pooler MR (2020) Using acetone for rapid PCR-amplifiable DNA extraction from recalcitrant woody plant taxa. Appl Plant Sci **8:** e11403

Guo W, Chen L, Chen H, Yang H, You Q, Bao A, Chen S, Hao Q, Huang Y, Qiu D, Shan Z, Yang Z, Yuan S, Zhang C, Zhang X, Jiao Y, Tran LP, Zhou X, Cao D (2020) Overexpression of GmWRI1b in soybean stably improves plant architecture and associated yield parameters, and increases total seed oil production under field conditions. Plant Biotechnol J **18:** 1639-1641

Hay J, Shi H, Heinzel N, Hebbelmann I, Rolletschek H, Schwender J (2014) Integration of a constraint-based metabolic model of Brassica napus developing seeds with 13C-Metabolic Flux Analysis. Frontiers in Plant Science **5:724**

Hojilla-Evangelista MP, Selling GW, Berhow MA, Evangelista RL (2014) Preparation, composition and functional properties of pennycress (Thlaspi arvense L.) seed protein isolates. Industrial Crops and Products **55:** 173-179

Ivarson E, Leiva-Eriksson N, Ahlman A, Kanagarajan S, Bulow L, Zhu LH (2016) Effects of Overexpression of WRI1 and Hemoglobin Genes on the Seed Oil Content of Lepidium campestre. Front Plant Sci **7:** 2032

Jako C, Kumar A, Wei Y, Zou J, Barton DL, Giblin EM, Covello PS, Taylor DC (2001) Seed-specific over-expression of an *Arabidopsis* cDNA encoding a diacylglycerol acyltransferase enhances seed oil content and seed weight. Plant Physiol **126:** 861-874

Jarvis BA, Romsdahl TB, McGinn MG, Nazarenus TJ, Cahoon EB, Chapman KD, Sedbrook JC (2021) CRISPR/Cas9-Induced fad2 and rod1 Mutations Stacked With fae1 Confer High Oleic Acid Seed Oil in Pennycress (Thlaspi arvense L.). Front Plant Sci **12:** 652319

Jo L, Pelletier JM, Goldberg RB, Harada JJ (2024) Genome-wide profiling of soybean WRINKLED1 transcription factor binding sites provides insight into seed storage lipid biosynthesis. Proc Natl Acad Sci U S A **121:** e2415224121

Kanai M, Mano S, Kondo M, Hayashi M, Nishimura M (2016) Extension of oil biosynthesis during the mid-phase of seed development enhances oil content in Arabidopsis seeds. Plant Biotechnol J **14:** 1241-1250

Kennedy EP (1961) Biosynthesis of complex lipids. Fed Proc **20:** 934-940

Kim D, Paggi JM, Park C, Bennett C, Salzberg SL (2019) Graph-based genome alignment and genotyping with HISAT2 and HISAT-genotype. Nat Biotechnol **37:** 907-915

Kim HJ, Silva JE, Iskandarov U, Andersson M, Cahoon RE, Mockaitis K, Cahoon EB (2015) Structurally divergent lysophosphatidic acid acyltransferases with high selectivity for saturated medium chain fatty acids from Cuphea seeds. Plant J **84:** 1021-1033

Kim MJ, Jang IC, Chua NH (2016) The Mediator Complex MED15 Subunit Mediates Activation of Downstream Lipid-Related Genes by the WRINKLED1 Transcription Factor. Plant Physiol **171:** 1951-1964

Koley S, Jyoti P, Lingwan M, Wei M, Xu C, Chu KL, Williams RB, Koo AJ, Thelen JJ, Xu D, Allen DK (2025) Persistent fatty acid catabolism during plant oil synthesis. Cell Reports **44:** 115492

Kruger NJ, Masakapalli SK, Ratcliffe RG (2011) Strategies for investigating the plant metabolic network with steady-state metabolic flux analysis: lessons from an Arabidopsis cell culture and other systems. Journal of experimental botany

Kuczynski C, McCorkle S, Keereetaweep J, Shanklin J, Schwender J (2022) An expanded role for the transcription factor WRINKLED1 in the biosynthesis of triacylglycerols during seed development. Front Plant Sci **13:** 955589

Lee EJ, Oh M, Hwang JU, Li-Beisson Y, Nishida I, Lee Y (2017) Seed-Specific Overexpression of the Pyruvate Transporter BASS2 Increases Oil Content in Arabidopsis Seeds. Front Plant Sci **8:** 194

Lee KR, Park ME, Kim HU (2024) Domestication and engineering of pennycress (Thlaspi arvense L.): challenges and opportunities for sustainable bio-based feedstocks. Planta **260:** 127

Leprince O, Pellizzaro A, Berriri S, Buitink J (2017) Late seed maturation: drying without dying. J Exp Bot **68:** 827-841

Li-Beisson Y, Shorrosh B, Beisson F, Andersson MX, Arondel V, Bates PD, Baud S, Bird D, Debono A, Durrett TP, Franke RB, Graham IA, Katayama K, Kelly AA, Larson T, Markham JE, Miquel M, Molina I, Nishida I, Rowland O, Samuels L, Schmid KM, Wada H, Welti R, Xu C, Zallot R, Ohlrogge J (2013) Acyl-lipid metabolism. The Arabidopsis book / American Society of Plant Biologists **11:** e0161

Li Q, Shao J, Tang S, Shen Q, Wang T, Chen W, Hong Y (2015) Wrinkled1 Accelerates Flowering and Regulates Lipid Homeostasis between Oil Accumulation and Membrane Lipid Anabolism in. Front Plant Sci **6:** 1015

Li W, Wang L, Qi Y, Xie Y, Zhao W, Dang Z, Zhang J (2022) Overexpression of WRINKLED1 improves the weight and oil content in seeds of flax (Linum usitatissimum L.). Front Plant Sci **13:** 1003758

Liu J, Hua W, Zhan G, Wei F, Wang X, Liu G, Wang H (2010) Increasing seed mass and oil content in transgenic Arabidopsis by the overexpression of wri1-like gene from Brassica napus. Plant physiology and biochemistry **48:** 9-15

Livak KJ, Schmittgen TD (2001) Analysis of relative gene expression data using real-time quantitative PCR and the 2(-Delta Delta C(T)) Method. Methods **25:** 402-408

Long CP, Antoniewicz MR (2019) High-resolution (13)C metabolic flux analysis. Nat Protoc **14:** 2856-2877

Lonien J, Schwender J (2009) Analysis of metabolic flux phenotypes for two Arabidopsis mutants with severe impairment in seed storage lipid synthesis. Plant Physiol **151:** 1617-1634

Love MI, Huber W, Anders S (2014) Moderated estimation of fold change and dispersion for RNA-seq data with DESeq2. Genome Biol **15:** 550

Lu C, Xin Z, Ren Z, Miquel M, Browse J (2009) An enzyme regulating triacylglycerol composition is encoded by the ROD1 gene of Arabidopsis. Proceedings of the National Academy of Sciences of the United States of America **106:** 18837-18842

Maeo K, Tokuda T, Ayame A, Mitsui N, Kawai T, Tsukagoshi H, Ishiguro S, Nakamura K (2009) An AP2-type transcription factor, WRINKLED1, of Arabidopsis thaliana binds to the AW-box sequence conserved among proximal upstream regions of genes involved in fatty acid synthesis. The Plant journal **60:** 476-487

Mata AT, Jorge TF, Ferreira J, do Rosario Bronze M, Branco D, Fevereiro P, Araujo S, Antonio C (2016) Analysis of low abundant trehalose-6-phosphate and related metabolites in Medicago truncatula by hydrophilic interaction liquid chromatography-triple quadrupole mass spectrometry. J Chromatogr A **1477:** 30-38

McGinn M, Phippen WB, Chopra R, Bansal S, Jarvis BA, Phippen ME, Dorn KM, Esfahanian M, Nazarenus TJ, Cahoon EB, Durrett TP, Marks MD, Sedbrook JC (2019) Molecular tools enabling pennycress (Thlaspi arvense) as a model plant and oilseed cash cover crop. Plant Biotechnol J **17:** 776-788

Misra A, Khan K, Niranjan A, Nath P, Sane VA (2013) Over-expression of JcDGAT1 from Jatropha curcas increases seed oil levels and alters oil quality in transgenic Arabidopsis thaliana. Phytochemistry **96:** 37-45

Mukherjee T, Kambhampati S, Morley SA, Durrett TP, Allen DK (2024) Metabolic flux analysis to increase oil in seeds. Plant Physiology

Napier JA, Haslam RP, Beaudoin F, Cahoon EB (2014) Understanding and manipulating plant lipid composition: Metabolic engineering leads the way. Curr Opin Plant Biol **19:** 68-75

Narvaez-Rivas M, Zhang Q (2016) Comprehensive untargeted lipidomic analysis using core-shell C30 particle column and high field orbitrap mass spectrometer. J Chromatogr A **1440:** 123-134

Norton G, Harris JF (1975) Compositional changes in developing rape seed (*Brassica napus* L.). Planta **123:** 163-174

Nunn A, Rodriguez-Arevalo I, Tandukar Z, Frels K, Contreras-Garrido A, Carbonell-Bejerano P, Zhang P, Ramos Cruz D, Jandrasits K, Lanz C, Brusa A, Mirouze M, Dorn K, Galbraith DW, Jarvis BA, Sedbrook JC, Wyse DL, Otto C, Langenberger D, Stadler PF, Weigel D, Marks MD, Anderson JA, Becker C, Chopra R (2022) Chromosome-level Thlaspi arvense genome provides new tools for translational research and for a newly domesticated cash cover crop of the cooler climates. Plant Biotechnol J **20:** 944-963

O'Grady J, Schwender J, Shachar-Hill Y, Morgan JA (2012) Metabolic cartography: experimental quantification of metabolic fluxes from isotopic labelling studies. Journal of experimental botany **63:** 2293-2308

Pang Z, Lu Y, Zhou G, Hui F, Xu L, Viau C, Spigelman AF, MacDonald PE, Wishart DS, Li S, Xia J (2024) MetaboAnalyst 6.0: towards a unified platform for metabolomics data processing, analysis and interpretation. Nucleic Acids Res **52:** W398-W406

Pawlak M, Klupczynska A, Kokot ZJ, Matysiak J (2019) Extending Metabolomic Studies of Apis mellifera Venom: LC-MS-Based Targeted Analysis of Organic Acids. Toxins (Basel) **12**

Pelletier JM, Kwong RW, Park S, Le BH, Baden R, Cagliari A, Hashimoto M, Munoz MD, Fischer RL, Goldberg RB, Harada JJ (2017) LEC1 sequentially regulates the transcription of genes involved in diverse developmental processes during seed development. Proc Natl Acad Sci U S A **114:** E6710-E6719

Plaxton WC, Smith CR, Knowles VL (2002) Molecular and regulatory properties of leucoplast pyruvate kinase from Brassica napus (rapeseed) suspension cells. Arch Biochem Biophys **400:** 54-62

Ratcliffe RG, Shachar-Hill Y (2006) Measuring multiple fluxes through plant metabolic networks. Plant Journal **45:** 490-511

Rawsthorne S (2002) Carbon flux and fatty acid synthesis in plants. Prog Lipid Res **41:** 182-196

Rende U, Niittyla T, Moritz T (2019) Two-step derivatization for determination of sugar phosphates in plants by combined reversed phase chromatography/tandem mass spectrometry. Plant Methods **15**

Roesler K, Shen B, Bermudez E, Li C, Hunt J, Damude HG, Ripp KG, Everard JD, Booth JR, Castaneda L, Feng L, Meyer K (2016) An Improved Variant of Soybean Type 1 Diacylglycerol Acyltransferase Increases the Oil Content and Decreases the Soluble Carbohydrate Content of Soybeans. Plant Physiol **171:** 878-893

Rolletschek H, Mayer S, Boughton B, Wagner S, Ortleb S, Kiel C, Roessner U, Borisjuk L (2021) The metabolic environment of the developing embryo: A multidisciplinary approach on oilseed rapeseed. Journal of Plant Physiology **265:** 153505

Ruuska SA, Girke T, Benning C, Ohlrogge JB (2002) Contrapuntal networks of gene expression during *Arabidopsis* seed filling. Plant Cell **14:** 1191-1206

Ruuska SA, Schwender J, Ohlrogge JB (2004) The capacity of green oilseeds to utilize photosynthesis to drive biosynthetic processes. Plant Physiol **136:** 2700-2709

Sagun JV, Yadav UP, Alonso AP (2023) Progress in understanding and improving oil content and quality in seeds. Front Plant Sci **14:** 1116894

Schneider CA, Rasband WS, Eliceiri KW (2012) NIH Image to ImageJ: 25 years of image analysis. Nature Methods **9:** 671-675

Schwacke R, Ponce-Soto GY, Krause K, Bolger AM, Arsova B, Hallab A, Gruden K, Stitt M, Bolger ME, Usadel B (2019) MapMan4: A Refined Protein Classification and Annotation Framework Applicable to Multi-Omics Data Analysis. Molecular Plant **12:** 879-892

Schwender J (2025) Resolving cofactor imbalance in triacylglycerol biosynthesis in oilseeds through glycolytic shunts: a modeling study. bioRxiv**:** 2025.2007.2031.667993

Schwender J, Goffman F, Ohlrogge JB, Shachar-Hill Y (2004) Rubisco without the Calvin cycle improves the carbon efficiency of developing green seeds. Nature **432:** 779-782

Schwender J, Hay JO (2012) Predictive Modeling of Biomass Component Tradeoffs in Brassica napus Developing Oilseeds Based on in Silico Manipulation of Storage Metabolism. Plant physiology **160:** 1218-1236

Schwender J, Hebbelmann I, Heinzel N, Hildebrandt T, Rogers A, Naik D, Klapperstuck M, Braun HP, Schreiber F, Denolf P, Borisjuk L, Rolletschek H (2015) Quantitative Multilevel Analysis of

Central Metabolism in Developing Oilseeds of Oilseed Rape during in Vitro Culture. Plant Physiol **168:** 828-848

Schwender J, Ohlrogge JB (2002) Probing in vivo metabolism by stable isotope labeling of storage lipids and proteins in developing *Brassica napus* embryos. Plant Physiology **130:** 347-361

Schwender J, Shachar-Hill Y, Ohlrogge JB (2006) Mitochondrial metabolism in developing embryos of *Brassica napus*. Journal of Biological Chemistry **281:** 34040-34047

Shi H, Ernst E, Heinzel N, McCorkle S, Rolletschek H, Borisjuk L, Ortleb S, Martienssen R, Shanklin J, Schwender J (2023) Mechanisms of metabolic adaptation in the duckweed Lemna gibba: an integrated metabolic, transcriptomic and flux analysis. BMC Plant Biology **23:** 458

Shumate A, Wong B, Pertea G, Pertea M (2022) Improved transcriptome assembly using a hybrid of long and short reads with StringTie. PLoS Comput Biol **18:** e1009730

Smith RG, Gauthier DA, Dennis DT, Turpin DH (1992) Malate- and pyruvate-dependent fatty acid synthesis in leucoplasts from developing castor endosperm. Plant Physiol **98:** 1233-1238

Sokol S, Millard P, Portais JC (2012) influx_s: increasing numerical stability and precision for metabolic flux analysis in isotope labelling experiments. Bioinformatics **28:** 687-693

Tang S, Peng F, Tang Q, Liu Y, Xia H, Yao X, Lu S, Guo L (2022) BnaPPT1 is essential for chloroplast development and seed oil accumulation in Brassica napus. J Adv Res **42:** 29-40

To A, Joubes J, Barthole G, Lecureuil A, Scagnelli A, Jasinski S, Lepiniec L, Baud S (2012) WRINKLED transcription factors orchestrate tissue-specific regulation of fatty acid biosynthesis in Arabidopsis. Plant Cell **24:** 5007-5023

Tsogtbaatar E, Cocuron JC, Alonso AP (2020) Non-conventional pathways enable pennycress (Thlaspi arvense L.) embryos to achieve high efficiency of oil biosynthesis. J Exp Bot **71:** 3037-3051

van Erp H, Kelly AA, Menard G, Eastmond PJ (2014) Multigene engineering of triacylglycerol metabolism boosts seed oil content in Arabidopsis. Plant Physiol **165:** 30-36

Vanhercke T, El Tahchy A, Shrestha P, Zhou XR, Singh SP, Petrie JR (2013) Synergistic effect of WRI1 and DGAT1 coexpression on triacylglycerol biosynthesis in plants. FEBS letters **587:** 364-369

Velasco L, Goffman FD, Becker HC (1998) Variability for the fatty acid composition of the seed oil in a germplasm collection of the genus Brassica. Genetic Resources and Crop Evolution **45:** 371-382

Weber A, Flügge UI (2002) Interaction of cytosolic and plastidic nitrogen metabolism in plants. Journal of Experimental Botany **53:** 865-874

Weselake RJ, Fell DA, Wang X, Scofield S, Chen G, Harwood JL (2024) Increasing oil content in Brassica oilseed species. Progress in Lipid Research**:** 101306

Wu XL, Liu ZH, Hu ZH, Huang RZ (2014) BnWRI1 coordinates fatty acid biosynthesis and photosynthesis pathways during oil accumulation in rapeseed. J Integr Plant Biol **56:** 582-593

Wulfert S, Schilasky S, Krueger S (2020) Transcriptional and Biochemical Characterization of Cytosolic Pyruvate Kinases in Arabidopsis thaliana. Plants (Basel) **9**

Xu C, Shanklin J (2016) Triacylglycerol Metabolism, Function, and Accumulation in Plant Vegetative Tissues. Annu Rev Plant Biol **67:** 179-206

Zhang C, Cahoon RE, Hunter SC, Chen M, Han J, Cahoon EB (2013) Genetic and biochemical basis for alternative routes of tocotrienol biosynthesis for enhanced vitamin E antioxidant production. Plant J **73:** 628-639

Zhang M, Fan J, Taylor DC, Ohlrogge JB (2009) DGAT1 and PDAT1 acyltransferases have overlapping functions in Arabidopsis triacylglycerol biosynthesis and are essential for normal pollen and seed development. The Plant Cell **21:** 3885-3901

Zhang Z, Schwartz S, Wagner L, Miller W (2000) A greedy algorithm for aligning DNA sequences. J Comput Biol **7:** 203-214

Figures

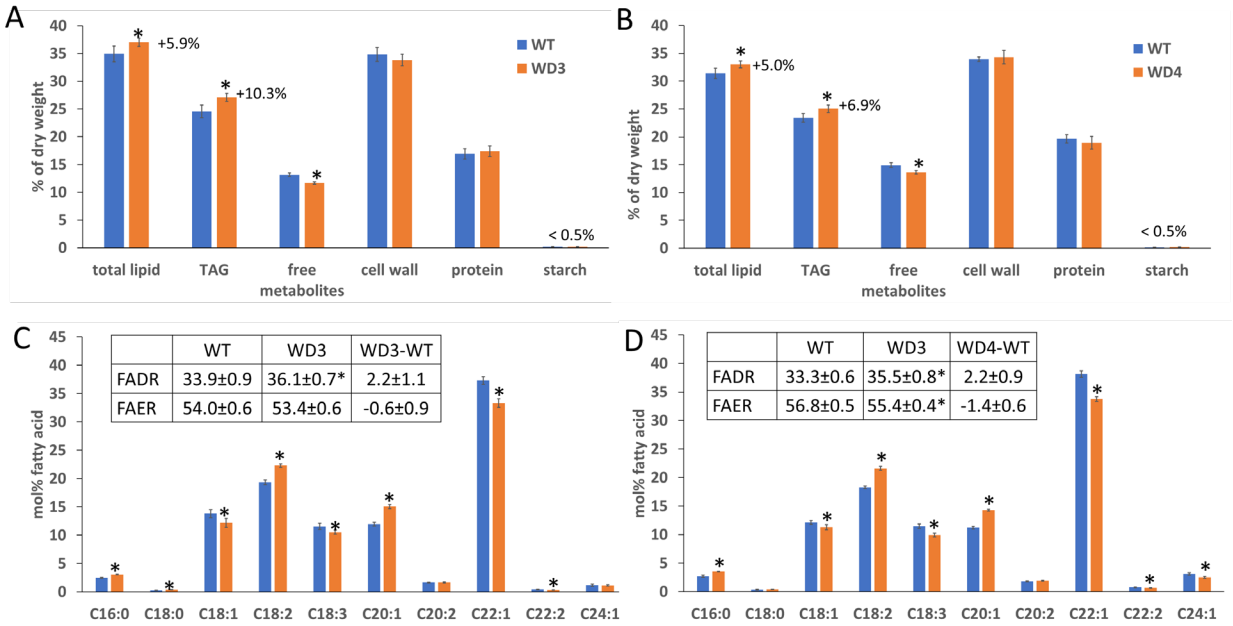

	WT	WD3	WD3-WT
FADR	33.9±0.9	36.1±0.7*	2.2±1.1
FAER	54.0±0.6	53.4±0.6	-0.6±0.9

	WT	WD3	WD4-WT
FADR	33.3±0.6	35.5±0.8*	2.2±0.9
FAER	56.8±0.5	55.4±0.4*	-1.4±0.6

Figure 1. Biomass composition and fatty acid composition of mature seeds of WT, WD3 (**A, C**) and WD4 (**B, D**). In panels **C**) and **D**) the total lipid fraction was analyzed. The fatty acid desaturation ratio (FADR) and fatty acid elongation ratio (FAER) were computed from the fatty acid profiles. WD3 and WD4 are independent WRI1/DGAT1 genetic crosses from different WRI1 and DGAT1 transgenic parent lines. The error bars represent the standard deviation from analysis of seeds from 10 plants (**A, D**) or 5 plants (**B, D**). Asterisks denote significant difference between WD3 and WT or WD4 and WT (two-sided Students t-test, $P < 0.01$). Free metabolites: methanol/water phase from biphasic chloroform/methanol/water solvent extraction. The full results are listed in Supplementary Table S1.

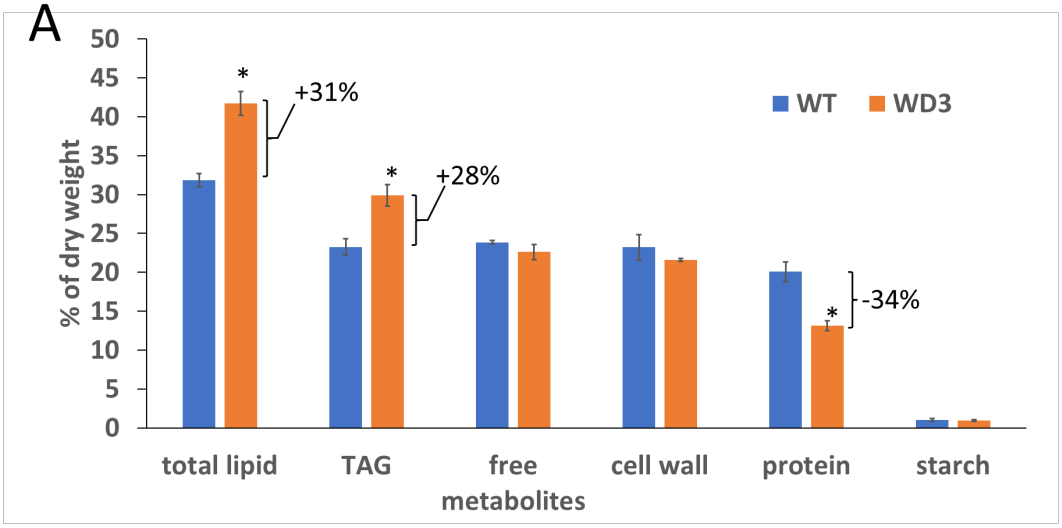

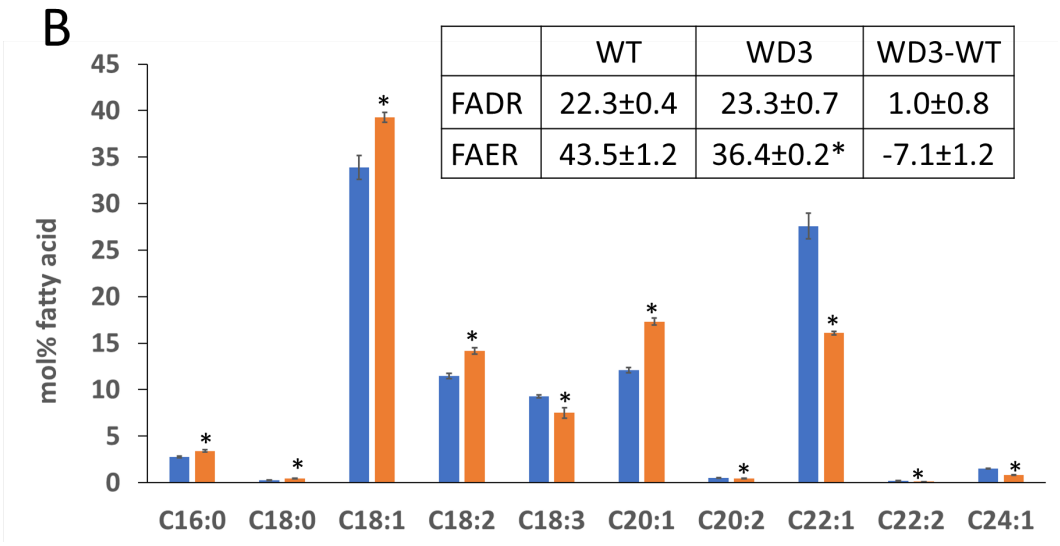

	WT	WD3	WD3-WT
FADR	22.3±0.4	23.3±0.7	1.0±0.8
FAER	43.5±1.2	36.4±0.2*	-7.1±1.2

Figure 2. Biomass composition (**A**) and fatty acid composition (**B**) of WT and WD3 embryos after 10 days in culture. In panel **B**) the total lipid fraction was analyzed. The fatty acid desaturation ratio (FADR) and fatty acid elongation ratio (FAER) were computed from the fatty acid profiles. Data represent mean ± standard deviation (n = 5). Asterisks denote significant difference between WD3 and WT (two-sided Students t-test, P < 0.01). Free metabolites: methanol/water phase from biphasic chloroform/methanol/water solvent extraction. The full results are listed in Supplementary Table S3.

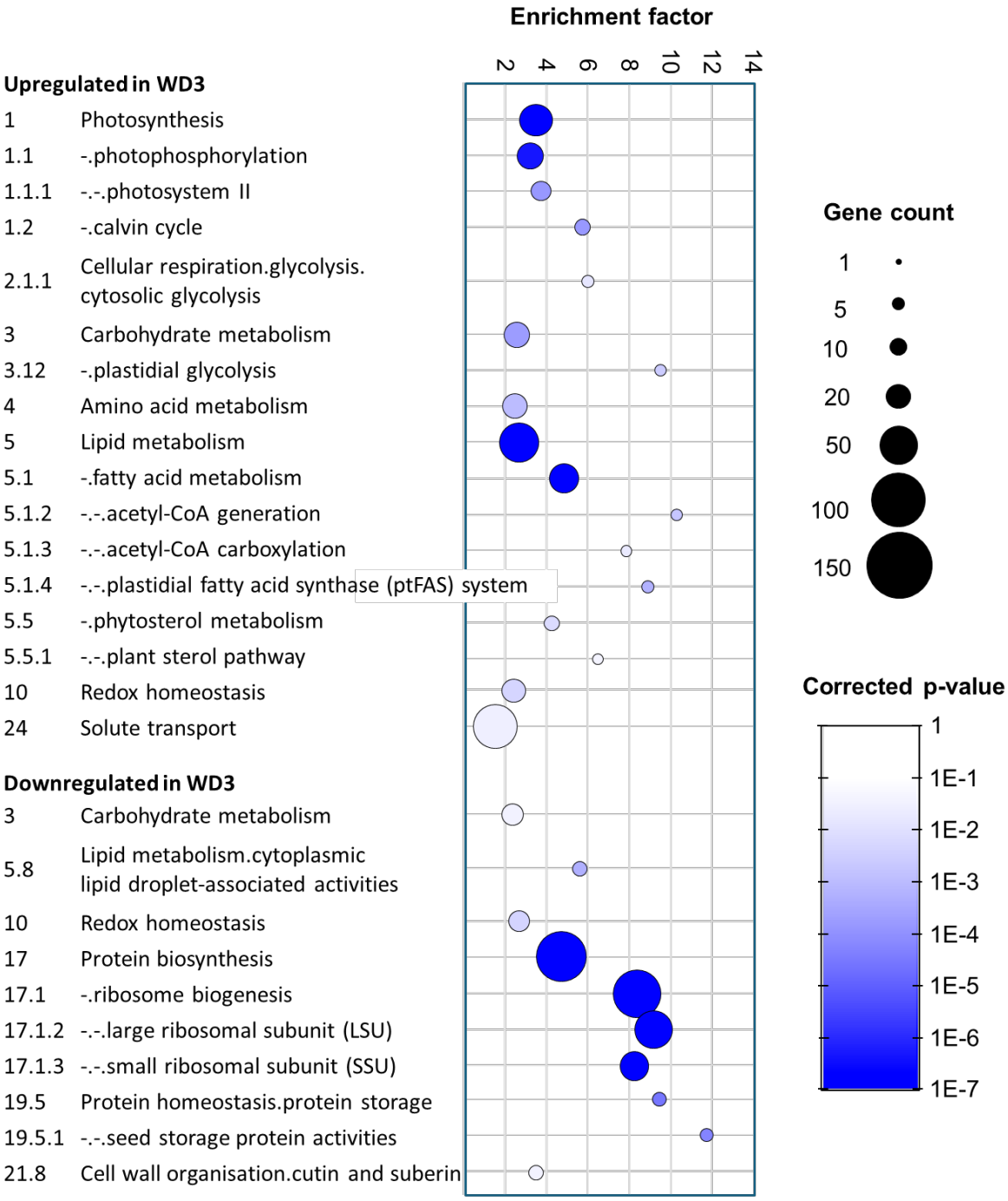

Figure 3. Mercator4 protein category (BIN) enrichment analysis of differentially expressed genes in cultured embryos. 1938 genes were up-regulated in WD3 relative to WT (up) and 1465 genes were down-regulated (down) were submitted to Mercator4 BIN enrichment analysis (Two-sided Fisher's exact test with overrepresentation analysis). Results were deemed significant for false discovery rate less than 0.05. Shown here are results for overrepresentation and up to bin level 3. The full results are listed in Supplementary Table S6.

	T	U
Ala	**3.52**	n/a
Arg	1.01	0.77
Asn	1.33	1.49
Asp	1.40	1.21
Cys	**1.84**	n/a
Gln	0.85	1.12
Glu	1.13	1.21
His	1.11	1.15
Ile	1.00	**1.67**
Leu	1.39	**2.33**
Lys	1.45	1.14
Met	1.17	n/a
Phe	**0.66**	**0.66**
Pro	**0.50**	**0.50**
Ser	**2.65**	1.15
Thr	1.31	1.04
Tyr	1.12	**1.52**
Val	1.37	**1.84**

	T	U
2-Ketoglutarate	n/a	**2.31**
cis-Aconitate	n/a	1.09
Citrate	1.31	1.11
Fumarate	n/a	**1.69**
Malate	**8.33**	**4.77**
Pyruvate	**1.53**	**2.92**
Succinate	n/a	**0.22**
Fructose	0.77	n/a
Glucose	0.94	n/a
Maltose	**0.45**	n/a
myo-inositol	**2.64**	n/a
Sucrose	**0.61**	n/a
2-phosphoglycerate	0.69	n/a
3-phosphoglycerate	0.89	0.88
Dihydroxyacetone-P	0.95	n/a
Erythrose 4-P	n/a	0.73
Fructose 6-P	**3.00**	**1.53**
Fructose 1,6-PP	n/a	**0.59**

	T	U
2-phosphoglycolate	0.99	n/a
Galactose 1-P	n/a	1.16
Glucosamine 6-P	n/a	0.87
Glucose 1-P	**2.70**	1.47
Glucose 6-P	1.47	**1.50**
Glyceraldehyde 3-P	**1.76**	n/a
Glycerol 3-P	n/a	1.27
Mannose 6-P	1.30	1.47
Phosphate	n/a	**0.64**
Phosphoenolpyruvate	n/a	1.35
Pyrophosphate	n/a	**0.61**
Sedoheptulose 1,7-PP	n/a	**0.54**
Sedoheptulose 7-P	n/a	0.94
Sorbitol 6-P	n/a	1.20
Sucrose 6-P	0.97	**0.66**
Thiamine-PP	0.96	n/a
Trehalose 6-P	1.16	**0.66**
UDP-glucose	0.72	1.19

	WD3/WT>1	WD3/WT<1
p-value > 5%		
2% < p-value ≤ 5%		
p-value ≤ 2%		

Figure 4. Fold-changes in the abundance of 54 metabolites of central metabolism between WD3 and WT. Results from targeted metabolomics (T) and untargeted metabolomics (U) obtained from separate embryo growth experiments were combined (Supplementary Table S10, Supplementary Table S11). Changes of 1.5-fold or more are highlighted in bold. The color coding represents p-values when WD3 is higher than WT (red) or vice versa (blue). n=8 for untargeted and n=4 for targeted metabolomics. 'n/a': No measurement.

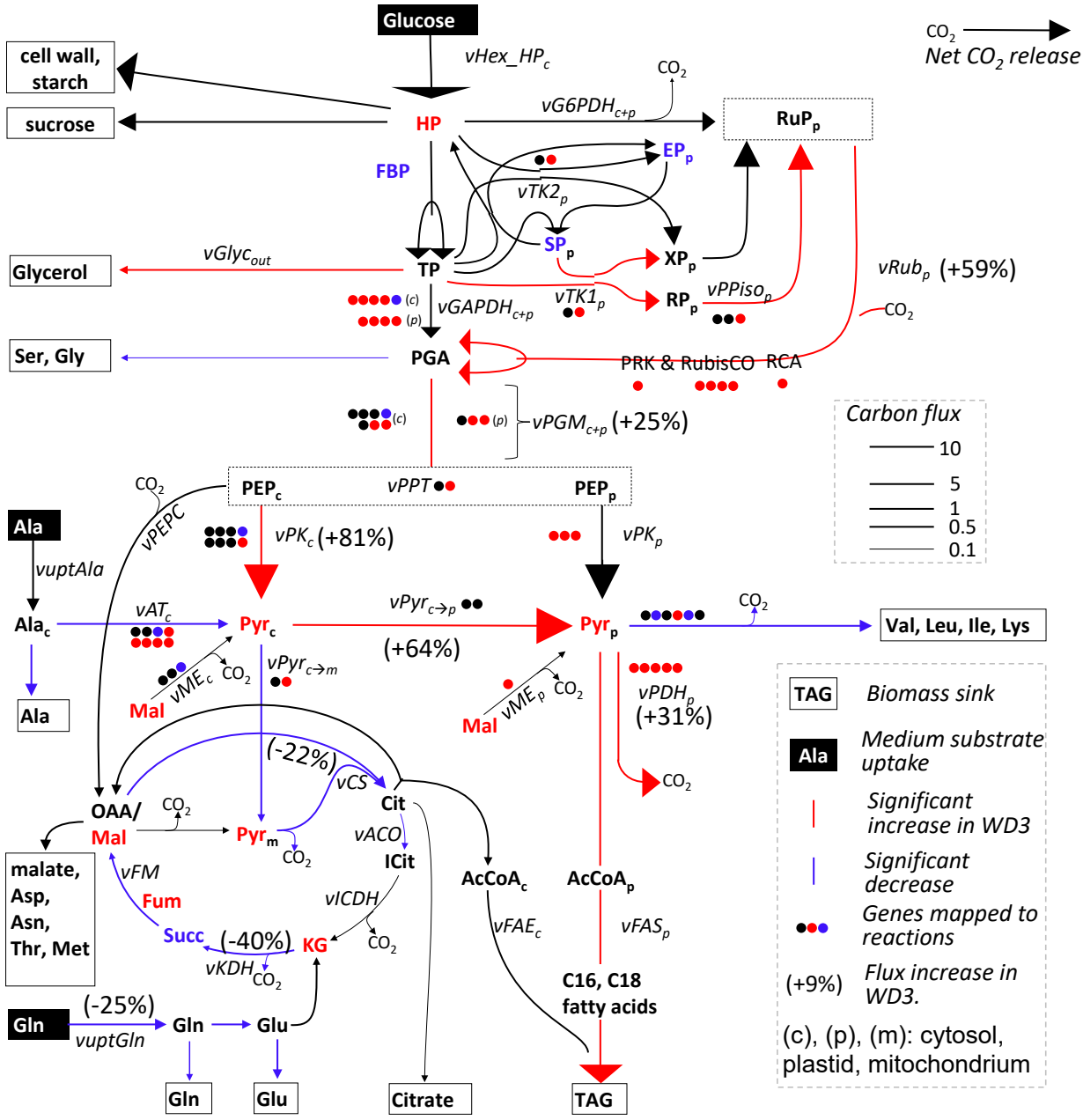

Figure 5. Comparative summary of metabolic flux, metabolite levels, and gene expression between in vitro cultured WT and WD3 embryos. Change in metabolite levels is derived from Figure 4 and is shown for a ≥1.5-fold change with p-value ≤ 5%. Genes are mapped only for reactions associated with the RubisCO shunt, lower glycolysis and the pyruvate node. Arrow thicknesses are proportional to mean carbon flux in WD3 (mol carbon gDW^{-1}). For all flux values see Supplementary Table S14. For metabolic network structure, reaction associated genes and gene expression information see Supplementary Table S21. Metabolite and gene names: AcCoA, acetyl-CoA; Cit, citrate; FBP, fructose bisphosphate; Fum, fumarate; HP, hexose phosphate; KG, 2-ketoglutarate; Mal, malate; PEP, phosphoenol pyruvate; PGA, 3-phosphoglycerate; PRK, phosphoribulokinase; Pyr, pyruvate; RCA, RubisCO activase; RP, ribose 5-phosphate; RuP, ribulose 5-phosphate; SP, sedoheptulose 7-phosphate; Succ, succinate; XP, xylulose 5-phosphate. Reaction abbreviations: vAco, aconitase; vAT_c, alanine amino transferase; vCS, citrate synthase; $vFAE_c$, cytosolic elongation of fatty acids; $vFAS_p$, plastidic fatty acid synthesis; $vglyc_{out}$, glycerol

3-phosphate into lipids; vFM, fumarase and malate dehydrogenase; $vG6PDH_{c+p}$, cytosolic and plastidic glucose 6-phosphate dehydrogenase; $vHex\text{-}HP_c$, uptake of glucose; vICDH, isocitrate dehydrogenase; vKDH, ketoglutarate dehydrogenase; vPEPC, phosphoenolpyruvate carboxylase; $vPGM_{c+p}$, combined cytosolic and plastidic phospho-glucomutase and enolase; $vPDH_p$, pyruvate dehydrogenase; vPK_c, cytosolic pyruvate kinase; vPK_p, plastidic pyruvate kinase; $vPyr_{cm}$, pyruvate import into mitochondria; $vPyr_{cp}$, pyruvate import into plastid; $vPPiso_p$, ribose-5-phosphate isomerase; vPPT, phosphoenolpyruvate/phosphate translocator; $vRub_p$, RubisCO; $vTK1_p$, transketolase 1; vuptAla, Ala uptake; vuptGln, Gln uptake.

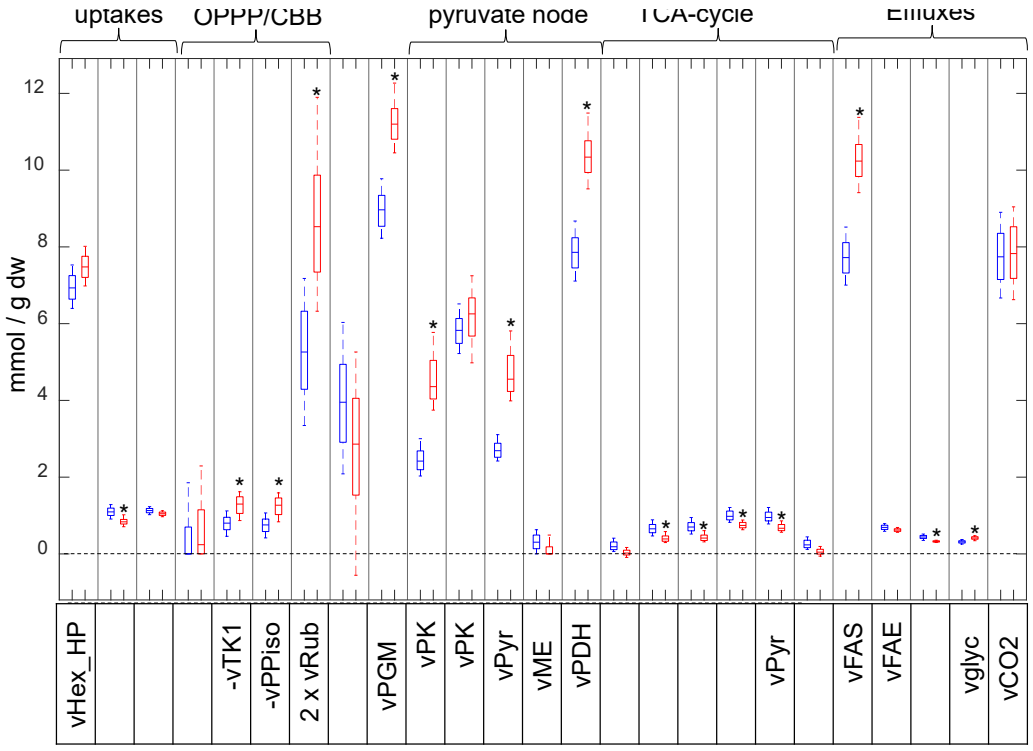

Figure 6. Range of flux estimates in growing WT (blue) and WD3 (red) pennycress embryos. 1000 Monte Carlo best fit solutions were sampled to determine the statistical uncertainty in flux values. Boxes show median and 95% confidence intervals and whiskers show the full range of the sampled flux values. Stars indicate significant differences (non-overlapping 95% confidence intervals). All fluxes are expressed on a molar basis relative to the formation of 1 g of dry weight. The complete flux data set is given in Supplementary Table S14. Subscripts *c*, *p*, *m* abbreviates for cytosol, plastid and mitochondria, respectively. Abbr.: BCAA+Lys, combined efflux of branched chain amino acids and Lys; OPPP/CBB, oxidative pentosephosphate / Calvin-Benson-Bassham cycle; TCA cycle, tricarboxylic acid cycle. Reaction abbreviations see Figure 5. vME_{c+p}, combined cytosolic and plastidic malic enzyme.